2021

Saturation Behaviors in Deep Turbulence

Jeffrey R. R. Beck
Michigan Technological University, jrbeck@mtu.edu

SATURATION BEHAVIORS IN DEEP TURBULENCE

By

Jeffrey R. Beck

A DISSERTATION

Submitted in partial fulfillment of the requirements for the degree of

DOCTOR OF PHILOSOPHY

In Electrical Engineering

MICHIGAN TECHNOLOGICAL UNIVERSITY

2021

This dissertation has been approved in partial fulfillment of the requirements for the Degree of DOCTOR OF PHILOSOPHY in Electrical Engineering.

Department of Electrical and Computer Engineering

Dissertation Advisor:	*Dr. Jeremy P. Bos*
Committee Member:	*Dr. Michael Roggemann*
Committee Member:	*Dr. Timothy Schulz*
Committee Member:	*Dr. Raymond Shaw*
Department Chair:	*Dr. Glen Archer*

Dedication

For Michelle, Joel, Heather, Fred, and Charles

Contents

List of Figures

List of Tables

Preface

This dissertation is mainly composed of three Journal articles authored by myself, my advisor, Dr. Jeremy Bos, and Dr. Mark Spencer. The first article appears in Chapter 2 was published [1] on November 18, 2020 in the Journal of the Optical Society of America A as "Angular anisoplanatism in non-Kolmogorov turbulence over horizontal paths." Dr. Bos is listed as a contributing author on this paper as he provided the initial idea for the paper and provided revisions. As first author, I performed all other contributing work and wrote and prepared the manuscript. I developed all of the analytical expressions and code for evaluating the anisoplanatic error. The content of Chapter 3 is in the final stages of preparation for submission to the Journal of the Optical Society of America A under the title "Angular anisoplanatism over horizontal and slant paths in non-Kolmogorov turbulence." This paper was written and prepared by myself with revisions by my advisor. The content in Chapter 4 is in the final stages of preparation for submission to Optical Engineering under the title "Effect of finite inner scale on the saturation behavior of branch-point density." Dr. Mark Spencer provided the initial idea and MATLAB code that I later modified for modelling branch-point density. I performed all work and prepared all portions of this chapter, except for the introduction which was authored by Dr. Spencer and revisions provided by Dr. Spencer and Dr. Bos. Terry Brennan provided access to and assistance with WavePlex. The work presented in this dissertation is the result

of my own effort strengthened by feedback and recommendations for improvement from Dr. Bos and Dr. Spencer.

Acknowledgments

First and foremost, I would like to thank my advisor Dr. Jeremy Bos, for his kind and patient guidance over the years we have worked together. He taught me not only the technical skills expected of someone with a Ph.D. in Electrical Engineering, but also the more esoteric skills (to me) like academic writing and navigating professional relationships.

Additionally, I would like to thank my academic support. To my committee members, I am grateful their time and helpful suggestions in improving my research. A big thank you also goes out to Dr. Mark Spencer of the Air Force Research Laboratory (AFRL), for giving me the opportunity to spend a summer out west on an exciting project. Without his direction and guidance, there would not be a fourth chapter in this dissertation. Dr. Christian Keyser deserves a chunk of credit (along with Dr. Bos) for convincing me to pursue a Ph.D. in Optics. Alongside the rest of the staff at AFRL's laser testing range at Eglin AFB, you all showed me how exciting and engaging research can be.

Thank you to all of my friends and colleagues at Michigan Tech and elsewhere for the thoughtful conversations, cups of coffee, pints of KBC, and laughs. Derek, Ian, Robert, Tanner, and all of the folks from Ridge Roamers, you made graduate school

the experience that it was and kept me going.

Lastly, none of this would be possible without Michelle Kelly and her patience, understanding, love, and companionship.

List of Abbreviations

This section may be removed if deemed unnecessary.

AO	Adaptive Optics
GBR	Guard Band Ratio
ISTAR	Intelligence, Surveillance, and Reconnaissance
LMSE	Least Mean Squared Error
LS	Least Squares
MSE	Mean Squared Error
MFBD	Multi-Frame Blind Deconvolution
OAM	Orbital Angular Momentum
SI	Speckle Imaging

Abstract

Distributed-volume atmospheric turbulence near the ground significantly limits the performance of incoherent imaging and coherent beam projection systems operating over long horizontal paths. Defense, military and civilian surveillance, border security, and target identification systems are interested in terrestrial imaging and beam projection over very long horizontal paths, but atmospheric turbulence can blur the imagery and aberrate the laser beam such that they are beyond usefulness. While many post-processing and adaptive optics techniques have been developed to mitigate the effects of turbulence, many of these techniques do not work as expected in stronger volumetric turbulence, or in many cases don't work at all. For these techniques to be effective or next generation techniques to be developed, a better theoretical understanding of deep turbulence is necessary. In an attempt to improve understanding of deep turbulence, this work explores the saturation behavior of two features of deep turbulence; the anisoplanatic error and the branch-point density.

In this work, the behavior of the anisoplanatic error over long horizontal and slant paths, where the angular extent of the scene is many times greater than the isoplanatic angle, is characterized by developing generalized expressions for the total, piston-removed, and piston-and-tilt-removed anisoplanatic error in non-Kolmogorov turbulence with a finite outer scale. As an outcome of this work it can be concluded

that in many cases the anisoplanatic error saturates to a value less than 1 rad^2. This means that while not actually infinite, the piston-removed and piston-and-tilt-removed isoplanatic angle is often significantly larger than expected. Additionally, power law exponent, outer scale size, scene geometry, and source model play a large part in determining the effective isoplanatic angle. The limit imposed on the system by the anisoplanatic error is much less severe than predicted by classical isoplanatic angle expression, but only if we include the interplay of piston and/or global tilt removal, a finite outer scale, accurate image formation models, and realistic turbulence profiles.

Additionally, in this work wave-optics simulations are used to model the branch-point density as a function of turbulence strength, sampling grid resolution, and inner scale. Another outcome of this work is that increasing grid resolution and turbulence strength cause the branch-point density to grow without bound, when no inner scale is used. When a non-zero inner scale is used, via a Hill spectrum, the growth of the branch-point density is significantly reduced as a function of increasing Rytov variance and saturates as a function of increasing inner scale.

Chapter 1

Introduction

It is well known that atmospheric turbulence limits the performance of imaging and beam control systems. Atmospheric temperature differences cause movement of the air mass and turbulent eddies. This results in randomly distributed differences in the index of refraction, which lead to phase aberrations in the optical wavefront. Additionally, light propagating through stronger turbulence or over longer distances will cause incoherent imagery to suffer from anisoplanatic and scintillation effects. In coherent beam projection these distortions lead to additional scintillation and wander. Because these aberrations are not only near the system's aperture, but distributed throughout the turbulent volume, this type of turbulence is known as distributed-volume turbulence. When this distributed-volume turbulence is especially strong, it is known as "deep" turbulence. In this case the resulting distortions will limit

the performance of any optical system operating in such a turbulent atmosphere, frequently causing the image to be so blurred or the laser beam to be so degraded that they are beyond usefulness. Unless seeing conditions are very good, the effects of deep turbulence will dominate most practical horizontal imaging situations.

A multitude of post-processing and Adaptive Optics (AO) techniques have been proposed and are currently being developed to counteract turbulence effects in practical horizontal imaging and beam control scenarios. These techniques have proven successful many times in weaker turbulence, but in stronger turbulence their efficacy and behavior often differ from what we expect to happen, or they fail to work altogether. This is because the forward models that inform these techniques are based upon analytical models built to describe the behavior of light propagating through weaker turbulence or correction within the isoplanatic patch. Scenarios where imaging and beam control systems are tasked with acquiring information about remote objects or focusing energy on a distant target are often near to the ground, over bodies of water, or in the upper atmosphere. In these cases, turbulence is often more severe than expected by our analytical models. To build effective post-processing and adaptive optics techniques in deep turbulence, this regime needs to be better characterized. To accomplish this, a better understanding of two important phenomena that occur in deep turbulence, anisoplanatism and branch points, is necessary.

The aim of this work is to examine the saturation behavior of the anisoplanatic error

and the behavior of the density of branch points that occur in deep turbulence. This is an effort to develop more accurate theory and expressions for imaging and beam control in deep turbulence. Efforts to better align theory with observed behavior lead to a better understanding of deep turbulence and an increased effectiveness in mitigated the effects of deep turbulence in imaging and beam control.

1.1 Deep Turbulence Problem

The impact of volumetric turbulence on imaging and beam control is governed by the propagation geometry and the distribution of turbulence between the object and the imaging system pupil; or, in the case of a laser beam, between the source and the target. There are three parameters commonly used to characterize the severity of turbulence, or conversely, the performance of imaging and beam control systems in turbulence. The isoplanatic angle[2], θ_0, the atmospheric coherence diameter, also known as Fried's parameter[2], r_0, and the plane-wave Rytov variance, also commonly known as the Rytov number, σ_R^2[3] . The Rytov variance specifically is a useful measure when talking about deep turbulence, because it physically represents the irradiance fluctuations associated with an unbounded plane wave propagating through a turbulent volume. Traditionally, studies of optical wave propagation are classified as either weak or strong fluctuation theories. When using the Kolmogorov spectrum definition of refractive index fluctuations, it is common to distinguish between weak

and strong fluctuation regimes with the Rytov variance. Weak fluctuations are associated with a Rytov variance $\sigma_R^2 < 0.5$, moderate fluctuations are characterized as $\sigma_R^2 = 0.5 \rightarrow 1.0$, and strong fluctuations are associated with $\sigma_R^2 > 1$. Deep turbulence is most often defined as volumetric optical turbulence where $\sigma_R^2 > 1$[4]. In addition to collected phase aberrations, strong volumetric turbulence gives rise to scintillation in the propagating optical wave front. Scintillation is a phenomenon caused by constructive and destructive interference in the complex optical field that looks like bright and dark spots in the irradiance of the wavefront after propagation. Due to strong scintillation and the distributed nature of volumetric turbulence two important phenomena are commonly encountered in deep turbulence: anisoplanatism and branch points.

1.1.1 Anisoplanatism

When conditions are isoplanatic, the light coming from all points in a scene or on an object can be assumed to experience similar turbulence induced changes in the atmospheric refractive index. Therefore all points also experience similar phase aberrations and distortions are shift-invariant across the region. Fried[2] first defined the isoplanatic angle θ_0 as the angular separation between point sources for which the phase changes at the aperture are considered significantly decorrelated and the distortions are now shift-variant across the region. However, in many horizontal and

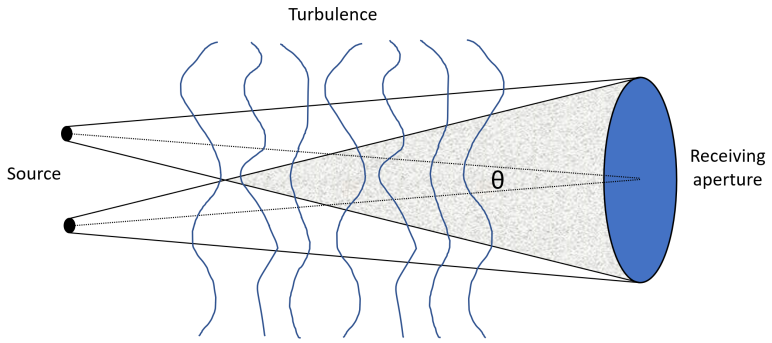

Figure 1.1: Angular anisoplanatism over a horizontal path

slant path imaging scenarios, it is reasonable to assume that the field of view of the imaging system will cover a wide enough angle to violate this assumption. In that case, we refer to the scenario as anisoplanatic.

Figure 1.1 shows the effect of anisoplanatism on two separate points in an imaged object, or in the case of AO an angularly separated source and reference beacon. As the optical path becomes longer and the turbulence increases in strength, the aberrations become more severe and the isoplanatic angle decreases. In guide star AO this means that as the angular separation between the reference beacon and the object increases, the performance of the AO system decreases[5]. In some cases to combat this, an artificial guide star[6, 7] or reference beacon can be pointed within the isoplanatic angle of the around the object to avoid the disadvantage of anisoplanatism. However, the effects of anisoplanatism still often remain in horizontal incoherent imaging where the object of interest often subtends an angle many times larger than the isoplanatic angle. In fact, in many horizontal imaging scenarios the isoplanatic angle can be on the order of the diffraction limit of the imaging system. Post-processing techniques

such as Speckle Imaging (SI), have been shown to work over angular extents many times the isoplanatic patch in highly anisoplanatic horizontal imaging scenarios. An attempt to explain the efficacy of these techniques in horizontal imaging is presented in Chapters 2 and 3.

1.1.2 Branch Points

Branch points traditionally arise when coherent light is propagated through distributed volume turbulence. Scintillation caused by optical turbulence produces small scale perturbations in the irradiance of an optical disturbance propagating through the atmosphere. These optical disturbances exist in two parts, both amplitude A and phase ϕ. The log-amplitude variance, also referred to as the Rytov variance, gives a measure of the strength of the scintillation experienced by coherent light. As the log-amplitude variance grows above ≈ 0.1 (for a plane wave), total destructive interference gives rise to corresponding discontinuities in the phase. This discontinuity takes on a value known as a residue, singularity, screw dislocation, optical vortex, or more commonly a branch point[8]. Branch points appear in pairs and result in branch cuts which show up as "cliffs" from $-\pi$ to π in the wrapped phase. These discontinuous changes in the phase due to branch cuts can't be fully compensated for by a continuous face-sheet deformable mirrors and thus pose a problem for AO systems[9].

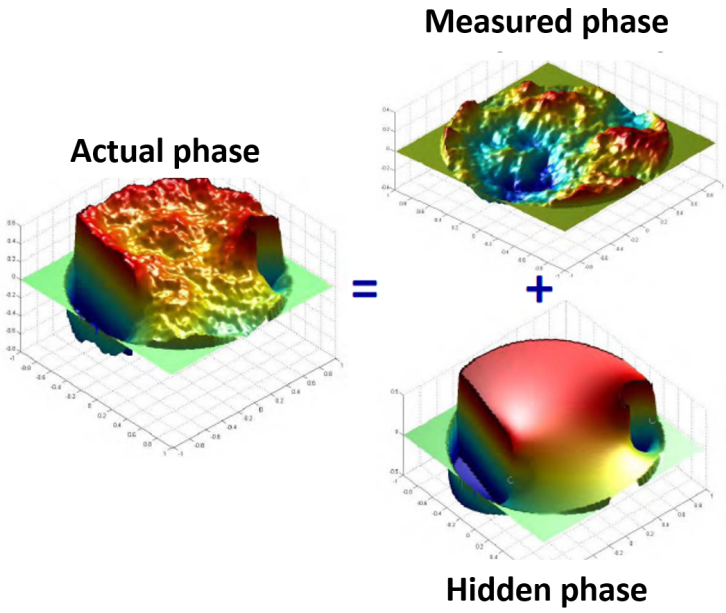

Figure 1.2: An example of the hidden phase component containing branch points and branch cuts. The hidden phase component is undetected by a Shack-Hartmann WFS. The actual phase is the phase that needs to be corrected for using phase compensation. The measured phase represents the LS reconstructed phase that is measured and corrected for using an AO system composed of a Shack-Hartmann WFS and a deformable mirror.

Using gradient-based wavefront sensing techniques like a Shack-Hartmann Wavefront Sensor (WFS), the phase of a wavefront cannot be directly measured, so an indirect reconstruction method must be used, such as least-squares (LS) reconstruction. When LS reconstruction is used a portion of the phase is left undetected. This portion is known as the hidden or rotational phase, seen in Fig. 1.2. The hidden phase exists as a consequence of mapping the wrapped phase to the real domain using LS reconstruction, which in turn maps the discontinuities to the null space[10]. Branch-point tolerant phase reconstruction algorithms have been developed[11, 12, 13], but the performance of these algorithms still needs to be quantified in hardware[14].

Voitsekhovich et. al[15] show that as optical turbulence strength increases, the number of branch points increases accordingly. In weak to moderate turbulence conditions branch points are minimal. However, in strong optical turbulence conditions consistent with deep turbulence, branch-point density has been observed to grow linearly without bound as a function of Rytov variance[16, 17]. If branch-points do grow without bound as turbulence strength increases, this poses a significant challenge for AO systems attempting beam control in deep turbulence. These works exclude the affect of several factors like finite inner and grid resolution on the density of branch points. An attempt to characterize the density of branch-points in deep turbulence is presented in Chapter 4.

1.2 Atmospheric Turbulence

1.2.1 Kolmogorov Turbulence

As the Sun shines on the Earth, energy is imparted unevenly into the ground. This uneven heating results in temperature inhomogeneities in the volume of air near the ground. On a large-scale the temperature differences between the warm air volume near the ground and the cooler air above it are resolved by convection. The convective movement of air generates turbulent eddies that can be characterized by their inner

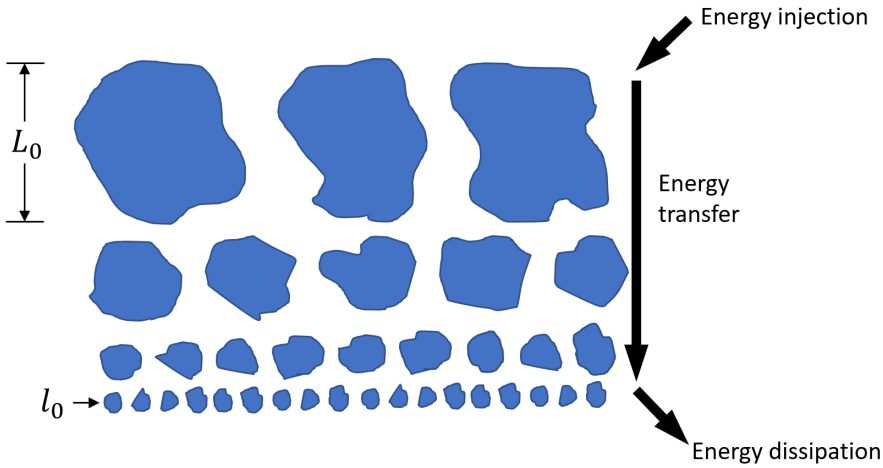

Figure 1.3: Depiction of the Kolmogorov cascade theory of turbulence. Here l_0 denotes the inner scale and L_0 denotes the outer scale. The eddies between the scale sizes make up the inertial subrange.

and outer scale sizes[18]. This structure can be visualized via Richardson's energy cascade theory of turbulence[19], sen in Fig. 1.3. The outer scale L_0 defines the largest eddy size and the inner scale l_0 defines the smallest eddy size. Eddies between the inner and outer scale are within the inertial subrange[18]. Eddies smaller than the inner scale are within the viscous dissipation range and become smaller and smaller until they eventually dissipate via molecular friction. This dissipation increases the temperature of the air volume. As the day progresses the Sun continually injects energy into this process, which increases the turbulence strength near the ground. This energy injection reaches a peak during midday and then decreases to a minimum at sunset when dissipation due to molecular friction exceeds the rate of energy injected into the system by solar heating. Over night turbulence conditions near the ground become unstable due to large scale events in the troposphere and this instability continues until sunrise when solar heating begins again and turbulence conditions

can stabilize to a minimum.

Turbulence near to the ground affects the propagation of light by randomly refracting said light as it travels through the volume of air. The temperature differences in the eddies that create movement of the air mass and turbulence also create random variations in the atmospheric index of refraction. The fluctuations in index of refraction are small, on the order of 10^{-6}, but the accumulation of these fluctuations over a long path can cause significant distortions on a propagating optical wave.

It is common to model the turbulence volume between a light source and a receiver or target as a random medium modelled so that the distribution of energy at different turbulence scale sizes reduces from outer scale sized inhomogeneities down to inner scale where molecular friction dominates. Mediums that conform to this model are referred to as power-law media. In the case where the roll-off in kinetic energy in the turbulence spectrum as a function of wavenumber between l_0 and L_0 has a slope of $-\frac{11}{3}$[20], the medium is referred to as a Kolmogorov medium[21]. Because the spatial power spectrum of refractive-index fluctuations is the same as that for temperature, and by extension the same spectral laws as velocity fluctuations, the spatial distribution of the turbulent kinetic energy spectrum can be directly related to variations in the index of refraction in the air. The well known Kolmogorov power-law spectrum

can be written as

$$\Phi_n(\kappa) = 0.033 C_n^2 \kappa^{-11/3}, 1/L_0 << \kappa << 1/l_0, \tag{1.1}$$

where C_n^2 is a structure function that describes the index of refraction with units of $m^{-2/3}$, κ is the scalar wave number[22].

1.2.2 Non-Kolmogorov Turbulence

To date, many works estimate the performance of imaging and laser systems assuming a Kolmogorov model for atmospheric turbulence. While this model has shown good agreement with experiments in the past, there is a growing body of work showing significant deviations from the Kolmogorov model in the upper atmosphere[23, 24], and near to the ground[25, 26, 27, 28]. Non-Kolmogorov turbulence is a turbulent media defined by an arbitrary power law α, where $\alpha = 11/3$ represents classical Kolmogorov turbulence. From [29], the three-dimensional non-Kolmogorov power spectrum for an arbitrary power law, α, can be defined as

$$\Phi_n(\kappa, \alpha, z) = \mathrm{A}[\alpha] \widetilde{C}_n^2(z) \left(\kappa^2 + \kappa_0^2\right)^{-\alpha/2}. \tag{1.2}$$

In Eq. (1.2), $\mathrm{A}[\alpha] = \frac{1}{4\pi^2} \cos(\pi\alpha/2)\Gamma[\alpha - 1]$ maintains consistency between the index

structure function and its power spectrum, $\widetilde{C}_n^2(z)$ is the structure constant, similar to $C_n^2(z)$, with units of $\mathrm{m}^{3-\alpha}$, $\Gamma[x]$ is Euler's gamma function, and $\kappa_0 = 2\pi/L_0$. When $\alpha = 11/3$, Eq. (1.2) reduces to the well known Kolmogorov turbulence spectrum in Eq. (1.1).

1.3 Summary of Key Results

In Chapter 2 expressions for the total, piston-removed, and piston-and-tilt-removed anisoplanatic error in non-Kolmogorov turbulence with a finite outer scale are developed. When these expressions were evaluated for turbulence strength, infinite and finite outer scale, and power-law exponents between 3 and 4 it was found that in many cases the anisoplanatic error saturated to a value less than 1 rad^2. As power-law increases and outer scale decreases more energy is in the piston and tilt terms, such that piston and tilt removal are likely to cause the anisoplanatic error to saturate as both the number of coherence cells across the aperture and the ratio of outer scale to aperture diameter approach unity.

In Chapter 3 the work in Chapter 2 was continued and the impact of a plane wave versus a spherical wave source model were compared and three different looking geometries were evaluated. Using a wavefront with a non-zero radius of curvature over a plane wavefront increased the effective isoplanatic angle for all cases by a factor of

≈ 6 regardless of outer scale size, turbulence strength, or power-law exponent. For the upward-looking slant path geometry the isoplanatic angle was 2-4 times larger than the horizontal case and the isoplanatic angle in the downward-looking case was 40-60% smaller than the horizontal case.

In Chapter 4 the branch-point density was characterized as a function of Rytov variance, grid resolution, and inner scale size. Increasing Rytov variance and grid resolution cause the branch-point density to increase without bound when no-inner scale is used. The growth of branch-point density is significantly limited with the presence of a finite inner scale.

1.4 Organization

The remainder of this dissertation is largely comprised of content from three journal articles which have either been accepted for publication in The Journal of the Optical Society of America A (JOSAA) or are in final preparation for submission at JOSA A and SPIE Optical Engineering. Alterations to formatting and language in the articles have been made where appropriate. Chapter 2 is derived from "Angular Anisoplanatism in Non-Kolmogorov Turbulence Over Horizontal Paths"[1], which was published online on November 18, 2020 in Journal of the Optical Society of America A (JOSA A). This paper provides an overview of the anisoplanatic error

saturation problem in horizontal imaging and key derivations of the anisoplanatic error used in Chapters 2 and 3. The content in Chapter 3 is in final preparation for submission to JOSA A under the title "Angular anisoplanatism over horizontal and slant paths in non-Kolmogorov turbulence" This paper extends the work in Chapter 2 by investigating the source type and the turbulence profile used in the anisoplanatic error expressions derived in Chapter 2. Characterization of the saturation behavior of branch-point density as a function of turbulence strength and resolution is found in Chapter 4. The content in Chapter 4 is in final preparation for submission to SPIE Optical Engineering under the title "Effect of finite inner scale on the saturation behavior of branch-point density." Chapter 5 contains a conclusion summarizing the discoveries in this body of work, and direction for further research.

Chapter 2

Angular Anisoplanatism in Non-Kolmogorov Turbulence Over Horizontal Paths

2.1 Introduction

In standoff imaging applications, image quality is reduced by atmospheric optical turbulence. A great body of work has focused on mitigating the effects of turbulence on imaging via Adaptive Optics (AO) and post-processing techniques. AO can provide nearly diffraction-limited imagery in a region around a natural or artificial guide star

referred to as the isoplanatic patch.

Techniques such as Speckle Imaging (SI) [30, 31, 32, 33], Multi-frame Blind Deconvolution (MFBD) [34, 35, 36, 37, 38], and Phase Diversity [39, 40, 41, 42] have also been used to correct imaging distortions within the isoplanatic patch. These techniques have also been used successfully over multiple isoplanatic patches [43, 44, 45]. In [43], Bos showed that these techniques can be used even when the isoplanatic angle is on the order of the diffraction-limited sampling rate of the telescope, when the integrated turbulence in terms of D/r_0, the ratio of the aperture size, D, to the Fried parameter, r_0, is small.

One explanation for the success of these techniques is that the definition of anisoplanatic error is overly pessimistic. Stone [46] argued that while piston and tilt contribute to the anisoplanatic error, they do not have an effect on image degradation. They show that if these contributions are removed, the anisoplanatic error often saturates.

Stone was concerned with astronomical imaging systems where typically $D/r_o > 10$. In previous work [47] we showed that this holds true in horizontal imaging scenarios where typically for sub-meter class telescopes $D/r_o < 10$. In this case the piston-removed anisoplanatic error often saturates to a value less than 1 rad^2. While the isoplanatic patch size is small, this means the piston-removed isoplanatic angle may be effectively infinite even though the imagery contains tip-tilt distortions.

Another explanation may be that the use of an infinite outer scale is affecting the anisoplanatic error expression. In many works [2, 48], including Stone's analysis [46], a Kolmogorov power spectrum with infinite outer scale and zero inner scale is assumed. This idealized spectrum is often used because it can provide tractable analytic solutions for quantities relevant to imaging and optical beam propagation. In this work focus is placed specifically on the outer scale. This is done because inner scale predominantly affects scintillation[49] and doesn't influence phase perturbations due to the filter function approach[50] removing small scale effects. However, outer scale is not removed by these filter functions and is therefore of interest here. In the idealized case, an infinite outer scale would need an infinite amount of energy in the turbulent spectrum, which is unphysical. Many works have demonstrated the impact of neglecting a finite outer scale in both theoretical and experimental settings [51, 52, 53]. This discrepancy can be accounted for mathematically by using a von Kármán spectrum [49], which includes the effect of a finite outer scale.

There is also a growing body of experimental observations of non-Kolmogorov turbulence in both the upper atmosphere [23, 24] and near to the ground [25, 26, 27, 28]. Non-Kolmogorov turbulence is a turbulent media defined by an arbitrary power law α, where $\alpha = 11/3$ represents classical Kolmogorov turbulence. In light of growing evidence of non-Kolmogorov turbulence, the behavior of anisoplanatism should be reevaluated in this context.

In this work, we reexamine Stone's analysis for horizontal paths with respect to several parameters. We investigate the effects of a finite outer scale and a non-Kolmogorov power law on the anisoplanatic error for smaller apertures. In this case D/r_0 is usually small, $D/r_0 < 10$, but it is common for imaging to be dominated by anisoplanatic distortions. In this paper we present analytical expressions for total anisoplanatic error in non-Kolmogorov turbulence with a finite outer scale and piston-removed and piston-and-tilt-removed anisoplanatic error. We find that in the presence of a finite outer scale, the piston-removed and piston-and-tilt-removed anisoplanatic error saturates to less than 1 rad^2 when $L_0/D \to 1$ and $D/r_0 < 10$.

The remainder of this paper proceeds as follows. In Section 2.2 we derive three general expressions for anisoplanatic error in non-Kolmogorov turbulence. The first expression is the total anisoplanatic error in non-Kolmogorov turbulence with a finite outer scale. The other two expressions are the anisoplanatic error due to piston and tilt. We subtract the later two separately and together to find the value of the piston-removed and piston-and-tilt-removed anisoplanatic error. All three expressions include a finite outer scale. In Section 2.3 we evaluate the effects of power law on the total and piston and tilt-removed anisoplanatic error expressions, along a horizontal path, as the ratio of aperture diameter to the Fried parameter, D/r_0 approaches unity. This analysis is repeated for the inclusion of a finite outer scale. The behavior of the anisoplanatic error is evaluated as the ratio of outer scale to aperture diameter, L_0/D, approaches unity. Conclusions and suggestions for future work are provided

in Section 2.4.

2.2 Derivation of Anisoplanatic Error Expressions

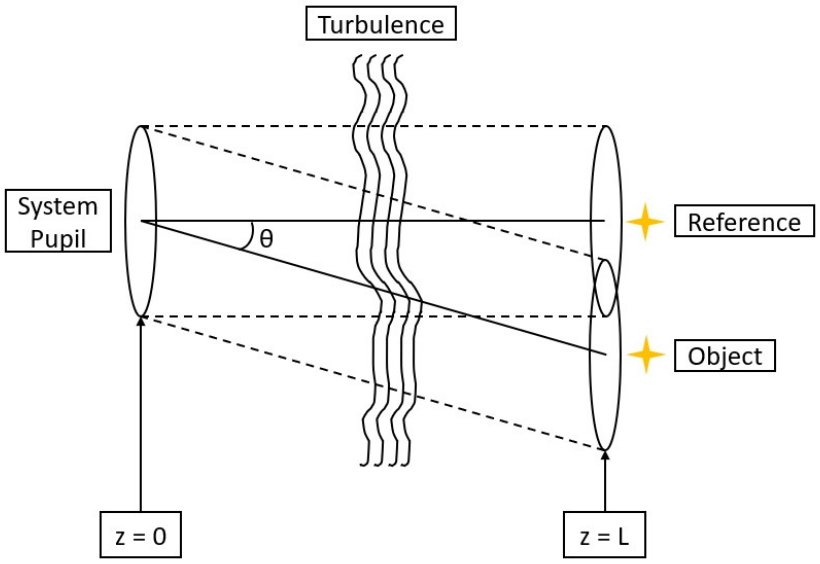

Figure 2.1: Horizontal propagation geometry, as viewed from above. Two wavefronts, the beacon and the object, are angularly separated. The angular separation leads to differing paths traveled by each wavefront, degrading the performance of phase correction.

In this section we develop an expression for the piston and tilt removed differential phase variance between two wavefronts as they propagate over a horizontal path from the imaging system at 0 to the target at a distance L, seen in Fig. 2.1. This geometry is analogous to describing the anisoplanatic error encountered when imaging a target along a horizontal path. The two beams are angularly separated by θ, which leads to a difference in the turbulence-induced wavefront distortions. Here,

the isoplanatic angle is the largest angular separation between the object and the reference such that the anisoplanatic error is equal to 1 rad^2. As the anisoplanatic error increases, atmospheric distortions become independent across the scene. The resulting wavefront error increases monotonically as a function of angle. The geometry in Fig. 2.1 is analogous to describing the anisoplanatic error when imaging a target along a long horizontal path.

Sasiela and Shelton [54] proposed that the effect of turbulence on imaging and beam propagation can be described by the proper combination of transverse spectral filter functions. Using this approach, we can begin with the general expression for angular differential phase variance, or anisoplanatic error, σ_ϕ^2, between two beams provided by Sasiela[50, p. 50,Eq. 2.107,] as

$$\begin{aligned}\sigma_\phi^2 = 2\pi k_0^2 \int_0^L \mathrm{d}z \int_0^\infty \mathrm{d}\vec{\kappa} f(\kappa) \\ \times \left(G_1(\gamma_1\vec{\kappa}) \cos\left[P_1(\gamma_1,\kappa,z)\right] - H(\vec{\kappa},z)\, G_2(\gamma_2\vec{\kappa}) \cos\left[P_2(\gamma_2,\kappa,z)\right]\right) \\ \times G_1^*(\gamma_1\vec{\kappa}) \cos\left[P_1(\gamma_1,\kappa,z)\right] - H^*(\vec{\kappa},z)\, G_2^*(\gamma_2\vec{\kappa}) \cos\left[P_2(\gamma_2,\kappa,z)\right],\end{aligned} \tag{2.1}$$

where $f(\kappa)$ is the normalized three-dimensional turbulence spectrum, $\vec{\kappa}$ is the two dimensional spatial frequency domain coordinate, L is the length of the propagation path, and $k = 2\pi/\lambda$ is the optical wavenumber. The P_n terms in Eq. (2.1) are the

diffraction parameters for each wave defined for propagation from $z = 0$ to $z = L$ as

$$P_n\left(\gamma_n, \kappa, z\right) = \frac{\gamma_n \kappa^2 \left(L - z\right)}{2k_0}, \tag{2.2}$$

where $\gamma_1 = \gamma_2 = \gamma = 1$ for two identical plane waves. $G_n(\gamma_n \vec{\kappa})$ is the complex aperture filter function for each beam, and $H(\vec{\kappa}, z)$ is the relative amplitude between the two waves. Furthermore, we consider that a vector separation between beam centers in real space, $\vec{d}$, is equivalent to a phase shift in transform space, allowing us to define the relative amplitude difference between waves for angular separation as $H\left[\vec{\kappa}, z\right] = \exp\left(i\gamma\vec{\kappa} \cdot \vec{d}\right)$. This can be used to simplify Eq. (2.1) as

$$\begin{aligned}
\sigma_\phi^2 = {} & 2\pi k_0^2 \int_0^L \mathrm{d}z \int_0^\infty \mathrm{d}\vec{\kappa} f\left(\kappa\right) \\
& \times \left(G_1\left(\vec{\kappa}\right) \cos\left[P_1\left(1, \kappa, z\right)\right] - \exp\left(i\gamma\vec{\kappa} \cdot \vec{d}\right) G_2\left(\vec{\kappa}\right) \cos\left[P_2\left(1, \kappa, z\right)\right]\right) \\
& \times G_1^*\left(\vec{\kappa}\right) \cos\left[P_1\left(1, \kappa, z\right)\right] - \exp\left(-i\gamma\vec{\kappa} \cdot \vec{d}\right) G_2^*\left(\vec{\kappa}\right) \cos\left[P_2\left(1, \kappa, z\right)\right],
\end{aligned} \tag{2.3}$$

The three-dimensional non-Kolmogorov power spectrum for an arbitrary power law, α, and a finite outer scale, L_0 can be defined as

$$\Phi_n\left(\kappa, \alpha, z\right) = \mathrm{A}\left[\alpha\right] \widetilde{C}_n^2(z) \left(\kappa^2 + \kappa_0^2\right)^{-\alpha/2}. \tag{2.4}$$

In Eq. (2.4), $\mathrm{A}\left[\alpha\right] = \frac{1}{4\pi^2} \cos(\pi\alpha/2)\Gamma\left[\alpha - 1\right]$ maintains consistency between the index structure function and its power spectrum, $\widetilde{C}_n^2(z)$ is the structure constant, similar to

$C_n^2(z)$, with units of $\mathrm{m}^{3-\alpha}$, $\Gamma[x]$ is Euler's gamma function, and $\kappa_0 = 2\pi/L_0$. When $\alpha = 11/3$ and $L_0 = \infty$, Eq. (2.4) reduces to the well known Kolmogorov turbulence spectrum, $\Phi_n(\kappa, z) = 0.033 C_n^2(z)\kappa^{-11/3}$. Equation (2.4) can be substituted into Eq. (2.3) to obtain

$$\begin{aligned}\sigma_\phi^2 = {} & 2\pi \mathrm{A}[\alpha] k_0^2 \int_0^L \mathrm{d}z \widetilde{C}_n^2(z) \int_0^\infty \mathrm{d}\vec{\kappa} \left(\kappa^2 + \kappa_0^2\right)^{-\alpha/2} \\ & \times \left(G_1(\vec{\kappa}) \cos\left[P_1(1, \kappa, z)\right] - \exp\left(i\gamma\vec{\kappa} \cdot \vec{d}\right) G_2(\vec{\kappa}) \cos\left[P_2(1, \kappa, z)\right]\right) \\ & \times \left(G_1^*(\vec{\kappa}) \cos\left[P_1(1, \kappa, z)\right] - \exp\left(-i\gamma\vec{\kappa} \cdot \vec{d}\right) G_2^*(\vec{\kappa}) \cos\left[P_2(1, \kappa, z)\right]\right).\end{aligned} \tag{2.5}$$

For compactness, we define $f(\vec{\kappa}, \alpha) = \left(\kappa^2 + \kappa_0^2\right)^{-\alpha/2}$ moving forward. From Sasiela [50] we can simplify Eq. (2.5) by defining the filter function as

$$F(\vec{\kappa}) = G(\vec{\kappa}) G^*(\vec{\kappa}). \tag{2.6}$$

This filter function can be set to different values depending upon if the total phase variance is of interest or if only the piston, tip/tilt, or greater order contributions are desired. Equation (2.6) can now be used to reduce Eq. (2.5) to

$$\begin{aligned}\sigma_\phi^2(\alpha) = {} & 2\pi \mathrm{A}[\alpha] k_0^2 \int_0^L \mathrm{d}z \widetilde{C}_n^2(z) \int_0^\infty \mathrm{d}\vec{\kappa} f(\kappa, \alpha) \\ & \times \left(\cos\left[P_1(1, \kappa, z)\right] - \exp\left(i\vec{\kappa} \cdot \vec{d}\right) \cos\left[P_2(1, \kappa, z)\right]\right)^2 F(\vec{\kappa}).\end{aligned} \tag{2.7}$$

We are interested only in finding the total phase variance so the filter function $F(\vec{\kappa})$

is set to one, reducing Eq. (2.7) to

$$\begin{aligned}\sigma_{\phi}^{2}(\alpha,\vec{d}) = 2\pi \mathrm{A}\left[\alpha\right] k_{0}^{2} \int_{0}^{L} \mathrm{d}z \widetilde{C}_{n}^{2}\left(z\right) \int_{0}^{\infty} \mathrm{d}\vec{\kappa} f\left(\kappa,\alpha\right) \\ \times \cos^{2}\left[\frac{\kappa^{2}\left(L-z\right)}{2k_{0}}\right] 2\left[1-\cos\left(\vec{\kappa}\cdot\vec{d}\right)\right]\end{aligned} \tag{2.8}$$

Here the $\cos^2$ term is the contribution of diffraction, which is very small for the scenarios of interest in this work. Moving forward, this term is neglected simplifying later evaluation. Assuming the turbulence is isotropic Eq. (2.8) can be rewritten in polar coordinates ρ and ζ and integrated over ζ such that

$$\begin{aligned}\sigma_{\phi}^{2}\left(\rho,\zeta,\alpha\right) = 2\left(2\pi\right) \mathrm{A}\left[\alpha\right] k_{0}^{2} \int_{0}^{L} \mathrm{d}z \widetilde{C}_{n}^{2}\left(z\right) \\ \times \int_{0}^{\infty} \int_{0}^{2\pi} \mathrm{d}\kappa \mathrm{d}\zeta \kappa f\left(\kappa,\alpha\right)\left(1-\cos\left(\kappa\rho\cos\left(\zeta\right)\right)\right).\end{aligned} \tag{2.9}$$

Using the identity [55], $2\pi \mathrm{J}_0\left(\kappa\rho\right) = \int_0^{2\pi} \cos\left(\kappa\rho\cos\zeta\right) \mathrm{d}\zeta$, the result of the integration is

$$\sigma_{\phi}^{2}\left(\rho,\alpha\right) = 2\left(2\pi\right)^{2} \mathrm{A}\left[\alpha\right] k_{0}^{2} \int_{0}^{L} \mathrm{d}z \widetilde{C}_{n}^{2}\left(z\right) \int_{0}^{\infty} \mathrm{d}\kappa \kappa f\left(\kappa,\alpha\right)\left(1-\mathrm{J}_{0}\left(\kappa\rho\right)\right). \tag{2.10}$$

When investigating angular anisoplanatism we are interested in the angular separation of the beams, θ. Replacing ρ with θz results in

$$\sigma_{\phi}^{2}\left(\theta,\alpha\right) = 2\left(2\pi\right)^{2} \mathrm{A}\left[\alpha\right] k_{0}^{2} \int_{0}^{L} \mathrm{d}z \widetilde{C}_{n}^{2}\left(z\right) \int_{0}^{\infty} \mathrm{d}\kappa \kappa f\left(\kappa,\alpha\right)\left(1-J_{0}\left(\kappa\theta z\right)\right). \tag{2.11}$$

Under the assumption of a constant turbulence strength $\widetilde{C}_n^2(z)$ along the path, we are interested in examining the relationship between an arbitrary characteristic length, $\hat{r}_0$, and the outer scale and their effect on the saturation of the anisoplanatic error. To accomplish this we recast Eq. **i**n terms of the non-Kolmogorov power spectrum $\Phi_\phi(\kappa, \alpha)$ in Appendix A.2 to get

$$\sigma_\phi^2(\theta, \alpha) = 4B(\alpha)c_1(\alpha) \int_0^L \mathrm{d}z \frac{\hat{r}_0^{2-\alpha}}{L} \int_0^\infty \mathrm{d}\kappa\kappa f(\kappa, \alpha) \left(1 - J_0(\kappa\theta z)\right). \tag{2.12}$$

Equation (2.12) is the total anisoplanatic error between two plane waves propagating through a turbulence volume of depth L with an arbitrary power law exponent α. Using methods outlined in Appendix A.3, we arrive at an analytical solution for Eq. (2.12) as

$$\sigma_\phi^2(\theta, \alpha) = 4B(\alpha)c_1(\alpha) \int_0^L \mathrm{d}z \frac{\hat{r}_0^{2-\alpha}}{L} \left(\frac{\kappa_0^{2-\alpha}}{-2+\alpha} - \frac{2^{1-\frac{\alpha}{2}} \left(\frac{\kappa_0}{\theta z}\right)^{1-\frac{\alpha}{2}} \mathrm{K}_{1-\frac{\alpha}{2}}\left[\theta z \kappa_0\right]}{\Gamma\left[\frac{\alpha}{2}\right]} \right) \tag{2.13}$$

Equation (2.12) provides the total anisoplanatic error, including the effect of piston and global tilt. In imaging scenarios we can ignore the effect of piston and global tilt on turbulence induced image degradation. Thus, we wish to examine the behavior of the anisoplanatic error with the effects of piston and tilt removed. We can calculate the phase variance due to piston by substituting the piston filter function [50]

$$F(\vec{\kappa}) = \left[\frac{2J_1(\kappa D/2)}{\kappa D/2} \right]^2, \tag{2.14}$$

into Eq. (2.7) and following the same derivation procedure to get

$$\begin{aligned}\sigma^2_{\phi,P}(\theta,\alpha) = 4B(\alpha)c_1(\alpha)\int_0^L \mathrm{d}z\frac{\hat{r}_0^{2-\alpha}}{L}\int_0^\infty \mathrm{d}\kappa\kappa f(\kappa,\alpha) \\ \times\left(1-J_0(\kappa\theta z)\right)\left[\frac{2J_1(\kappa D/2)}{\kappa D/2}\right]^2.\end{aligned} \tag{2.15}$$

We can repeat this process using the tilt filter function [50]

$$F(\vec{\kappa}) = \left[\frac{4J_2(\kappa D/2)}{\kappa D/2}\right]^2, \tag{2.16}$$

such that the phase variance due to tilt is

$$\begin{aligned}\sigma^2_{\phi}(\theta,\alpha) = 4B(\alpha)c_1(\alpha)\int_0^L \mathrm{d}z\frac{\hat{r}_0^{2-\alpha}}{L}\int_0^\infty \mathrm{d}\kappa\kappa f(\kappa,\alpha) \\ \times\left(1-J_0(\kappa\theta z)\right)\left(1-\left[\frac{2J_1(\kappa D/2)}{\kappa D/2}\right]^2-\left[\frac{4J_2(\kappa D/2)}{\kappa D/2}\right]^2\right).\end{aligned} \tag{2.17}$$

To get the phase variance due to the removal of piston and/or tilt all that must be done is to subtract Eqs. (2.15) and/or (2.17) from Eq. (2.13). We provide analytical expressions for both Eq. (2.15) and (2.17) in Appendices A.4 and A.5 respectively.

If we compare Eq. (2.12) to Stone's expression for anisoplanatic error between two plane waves by setting $\alpha = 11/3$ and neglecting outer scale, Eq. (2.12) reduces to

$$\sigma^2_{\phi}(\theta,\alpha) = 1.95935\int_0^L \mathrm{d}z\frac{\hat{r}_0^{-5/3}}{L}\int_0^\infty \mathrm{d}\kappa\kappa^{-8/3}\left(1-J_0(\kappa\theta z)\right). \tag{2.18}$$

From inspection it is obvious that this expression does not match Stone's[46, Eq. 29], but when numerically evaluated it provides identical results. From previous work [47] we know that Stone's expression, and by extension our expression, is valid for cases of constant turbulence over a horizontal propagation path.

2.3 Results

Now we explore the effect of a change in power law on the anisoplanatic error for a pair of horizontally propagating plane waves using the total and piston and tilt-removed expressions from the previous section. For all scenarios in this section the horizontal propagation distance $L = 1$ km and a wavelength of 500 nm was used.

First, we evaluate Eqs. (2.12), (2.15), and (2.17) in terms of the separation angle θ for three values of the power law, $\alpha = 3.1, 11/3$, and 3.9 and three values of $\hat{r_0}$ such that $D/\hat{r_0} = 1, 3$ and 9, seen in Fig. 2.2. The values of $\alpha = 3.1$ and $\alpha = 3.9$ were chosen to represent extreme deviations from the Kolmogorov value of $\alpha = 11/3$, as they are close to the limits of $\alpha = 3$ and $\alpha = 4$. Figure 2.2 is ordered such that left to right represents a change of α from 3.1 to 3.9 and top to bottom represents a change of $D/\hat{r_0}$ from 1 to 9. The isoplanatic angles for all cases can also be seen in Table. 2.1. We note that for some cases, marked with a shaded cell, the anisoplanatic error never reaches a value of 1 rad^2 and instead saturates to the specified value.

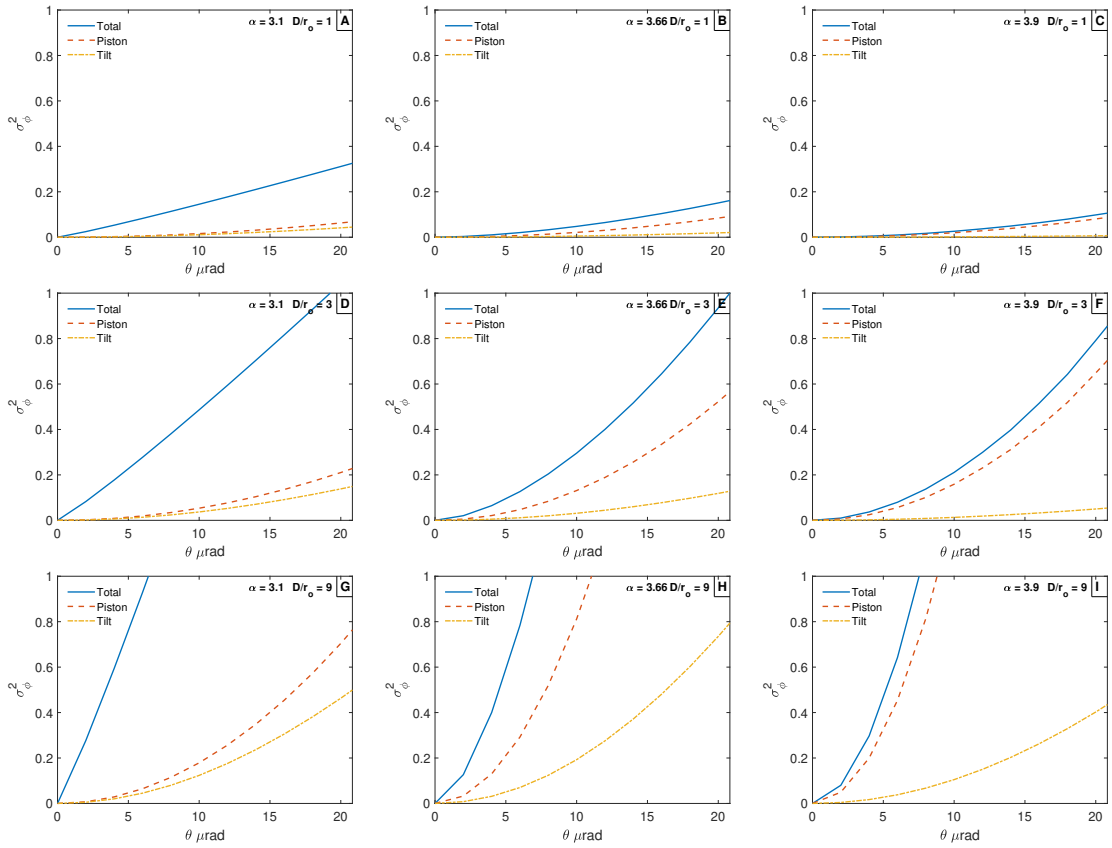

Figure 2.2: Anisoplanatic error as a function of θ for a fixed aperture size $D = 0.10$m along a horizontal path. Sub-figures organized as follows: **(A)** $\alpha = 3.1, D/\hat{r_0} = 1$ **(B)** $\alpha = 3.66, D/\hat{r_0} = 1$ **(C)** $\alpha = 3.9, D/\hat{r_0} = 1$ **(D)** $\alpha = 3.1, D/\hat{r_0} = 3$ **(E)** $\alpha = 3.66, D/\hat{r_0} = 3$ **(F)** $\alpha = 3.9, D/\hat{r_0} = 3$ **(G)** $\alpha = 3.1, D/\hat{r_0} = 9$ **(H)** $\alpha = 3.66, D/\hat{r_0} = 9$ **(I)** $\alpha = 3.9, D/\hat{r_0} = 9$.

From Fig. 2.2 it is evident that in all cases, removing contributions from piston decreases the anisoplanatic error. The magnitude of these contributions varies depending upon both the value of α and $D/\hat{r_0}$. In the case where the smallest change in isoplanatic angle occurs, $\alpha = 3.1$ and $D/\hat{r_0} = 9$, the removal of piston only decreases the isoplanatic angle by 0.5 μrads. The largest change in isoplanatic angle occurs when $\alpha = 3.9$ and $D/\hat{r_0} = 1$. Here, piston removal increases the isoplanatic angle from nearly 70 μrads to infinity, where the anisoplanatic error saturates to a value of

		D/r_0		
		1	3	9
α =3.1	Total	57.78	19.26	6.41
	Total-P	0.70	24.80	6.92
	Total-P-TLT	0.31	86.45	7.38
α =3.66	Total	62.5	20.82	6.90
	Total-P	0.28	44.74	9.85
	Total-P-TLT	0.09	0.55	11.66
α =3.9	Total	68.09	22.67	7.53
	Total-P	0.09	0.74	18.04
	Total-P-TLT	0.02	0.20	26.50

Table 2.1

Isoplanatic angles, in μradians, for varying power law and D/r_0 values. These results include the total isoplanatic angle, the piston-removed isoplanatic angle, and the piston and tilt removed isoplanatic angle for all cases of interest. The shaded box denotes a case where the anisoplanatic error, measured in rad^2, never reaches a value of 1 rad^2 and here it saturates to the specified anisoplanatic error.

0.09 rad^2. For all cases the removal of piston contributions increases the isoplanatic angle and as $D/\hat{r_0}$ approaches unity, it causes the anisoplanatic error to saturate to a value less than 1 rad^2.

The same trend continues when examining combined piston and tilt removal. When both piston and tilt are removed the isoplanatic angle saturates to some value less than 1 rad^2 as $D/\hat{r_0}$ approaches unity.

The values of D/r_0 we use here were selected to demonstrate the range of anisoplanatic error behavior when $D/r_0 < 10$. When $D/\hat{r_0} = 1$ the scenario is effectively a lower limit where the coherence length is as large as the aperture diameter. In this case turbulence has no effect on the image apart from tilt. When $D/\hat{r_0} = 3$ the scenario

represents a realistic imaging scenario with strong anisoplanatic turbulence, where $\hat{r_0} \approx 3$cm (when $D = 10$ cm). Finally, when $D/\hat{r_0} = 9$ regardless of piston or tilt removal, the anisoplanatic error never saturates. This may represent a limiting value on the value of $D/\hat{r_0}$ where anisoplanatism is more important than coherence.

Next, we again evaluate Eqs. (2.12), (2.15), and (2.17) in terms of the separation angle θ, but we include the addition of a finite outer scale. The analysis in Fig. 2.2 is repeated in Figs. 2.3 and 2.4, with a finite outer scale where $L_0/D = 10$ and 1 respectively. These outer scale values were selected to highlight behavior in two interesting scenarios. First, the case where $L_0/D = 10$ was chosen because here the outer scale is 1 m, which is a common estimate of the outer scale at ≈ 1 m above the ground. Secondly, the case where $L_0/D = 1$ was chosen because it represents the lower bound of behavior where the outer scale is on the order of the system's aperture diameter. This unity value allows us to look at the relationship between finite outer scale and anisoplanatism in the extreme. In Figs. 2.3 and 2.4 we also include the corresponding case where outer scale is infinite for comparison. The isoplanatic angles for all cases can be seen in Table. 2.2.

Figure 2.3 shows that the behavior of the anisoplanatic error is much the same as it is in the case of an infinite outer scale. The magnitude of the total anisoplanatic error, in the case of $D/\hat{r_0} = 3$, at 20 μrads is 90% of the infinite outer scale case when $\alpha = 3.1$ **(A)**, meanwhile, this value shrinks to 20% when $\alpha = 3.9$ **(C)**. Comparing

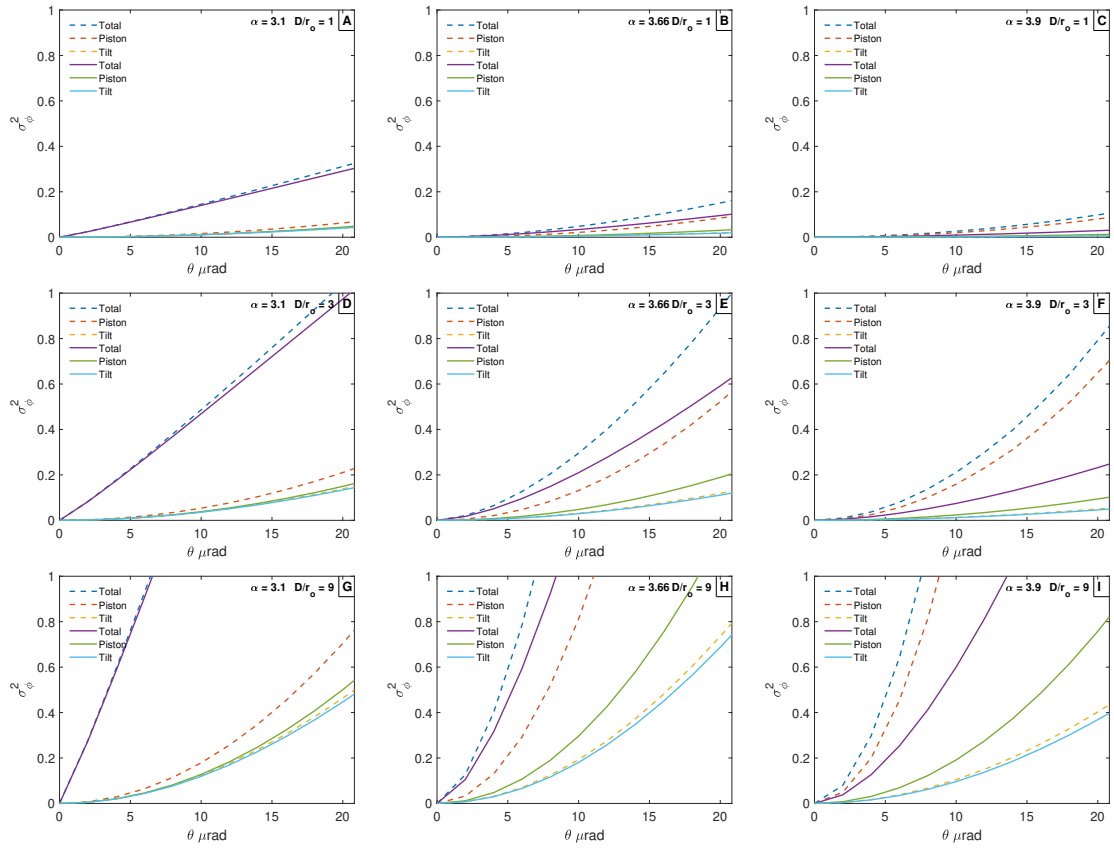

Figure 2.3: Anisoplanatic error as a function of θ for a fixed aperture size $D = 0.10$ m and values of $D/\hat{r_0} = 1, 3$, and 9, along a horizontal path. A finite outer scale of $L_0 = 1$ m corresponding to $L_0/D = 10$ is considered for all cases **(solid lines)**. Corresponding cases where $L_0 = \infty$ are included for comparison **(dashed lines)**. Sub-figures organized as follows:**(A)** $\alpha = 3.1, D/\hat{r_0} = 1$ **(B)** $\alpha = 3.66, D/\hat{r_0} = 1$ **(C)** $\alpha = 3.9, D/\hat{r_0} = 1$ **(D)** $\alpha = 3.1, D/\hat{r_0} = 3$ **(E)** $\alpha = 3.66, D/\hat{r_0} = 3$ **(F)** $\alpha = 3.9, D/\hat{r_0} = 3$ **(G)** $\alpha = 3.1, D/\hat{r_0} = 9$ **(H)** $\alpha = 3.66, D/\hat{r_0} = 9$ **(I)** $\alpha = 3.9, D/\hat{r_0} = 9$.

Tables 2.1 and 2.2, we see that for $L_0/D \geq 10$, at all values of α, with and without piston removal and combined piston and tilt removal, the isoplanatic angle is widened by several microradians at most. In the cases where the anisoplanatic error saturates to a value less than 1 rad^2 when $L_0 = \infty$, the inclusion of an outer scale where $L_0/D \geq 10$ has little impact on the magnitude of the saturation value.

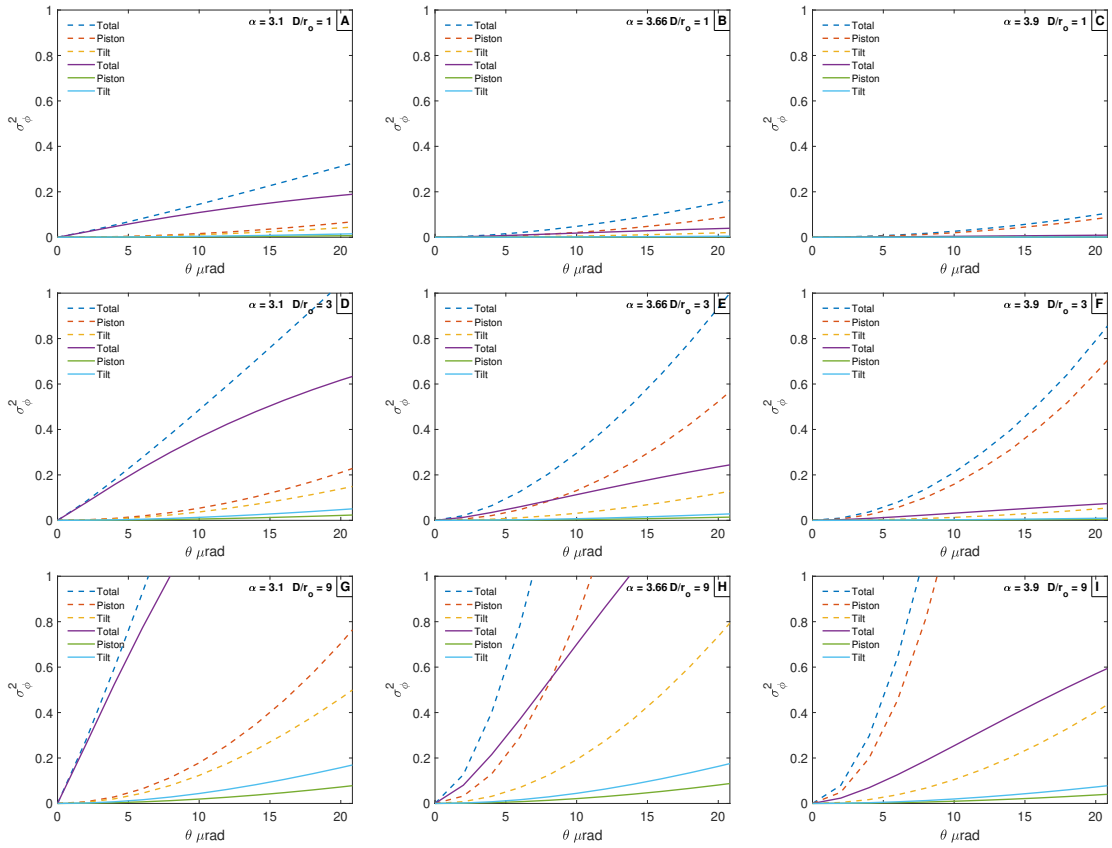

Figure 2.4: Anisoplanatic error as a function of θ for a fixed aperture size $D = 0.10$ m and values of $D/\hat{r_0} = 3, 5$, and 7, along a horizontal path. A finite outer scale of $L_0 = 0.1$ m corresponding to $L_0/D = 1$ is considered for all cases **(solid lines)**. Corresponding cases where $L_0 = \infty$ are included for comparison **(dashed lines)**. Sub-figures organized as follows:**(A)** $\alpha = 3.1, D/\hat{r_0} = 1$ **(B)** $\alpha = 3.66, D/\hat{r_0} = 1$ **(C)** $\alpha = 3.9, D/\hat{r_0} = 1$ **(D)** $\alpha = 3.1, D/\hat{r_0} = 3$ **(E)** $\alpha = 3.66, D/\hat{r_0} = 3$ **(F)** $\alpha = 3.9, D/\hat{r_0} = 3$ **(G)** $\alpha = 3.1, D/\hat{r_0} = 9$ **(H)** $\alpha = 3.66, D/\hat{r_0} = 9$ **(I)** $\alpha = 3.9, D/\hat{r_0} = 9$.

In Fig. 2.4 a value of $L_0/D = 1$ was used. Comparing Fig. 2.4 to Figs. 2.3 and 2.2 we see that the anisoplanatic error decreases in all cases as the outer scale becomes smaller. From Table 2.2 we see that when $L_0/D \to 1$ the smaller outer scale has a much larger impact on the isoplanatic angle when compared to the infinite outer scale case. Additionally, we see that the cases where the anisoplanatic error doesn't

		D/r_0					
		$L_0/D = 1$			$L_0/D = 10$		
		1	3	9	1	3	9
α =3.1	Total	0.23	0.78	8.54	74.16	20.85	6.60
	Total-P	0.21	0.70	8.59	0.60	27.69	6.96
	Total-P-T	0.18	0.59	8.87	0.30	46.63	7.40
α =3.66	Total	0.06	0.35	15.87	13.21	29.85	8.55
	Total-P	0.10	0.30	15.35	0.29	47.85	10.01
	Total-P-T	0.04	0.23	18.05	0.09	0.54	11.73
α =3.9	Total	0.01	0.11	0.90	0.57	55.04	14.03
	Total-P	0.01	0.09	0.75	0.10	0.78	18.62
	Total-P-T	0.01	0.07	0.55	0.02	0.19	26.95

Table 2.2
Isoplanatic angles, in μradians, for varying power law and L_0/D values. Similar to Table. 2.1, the shaded box denotes a case where the anisoplanatic error never reaches a value of 1 rad^2 and here it saturates to the specified anisoplanatic error.

saturate occur when the power law exponent is smaller than $\alpha = 11/3$ and there is no piston or tilt removal. In all other cases, the anisoplanatic error saturates to a value less than 1 rad^2. In effect, these observations show that the piston-removed and piston-and-tilt-removed anisoplanatic error saturates to a value less than 1 rad^2 as L_0/D approaches unity and D/r_0 approaches unity.

2.4 Conclusion

We have derived generalized expressions for the total and piston-and-tilt-removed anisoplanatic error in the case of two angularly-separated, horizontally-propagating, plane waves with identical circular apertures. While this expression is valid only for

plane waves, in a standoff imaging scenario, we expect the results to hold for a more realistic spherical wave case and apply broadly to imaging problems. We numerically evaluated these expressions for changing power-law media with exponents between 3 and 4, for both finite and infinite outer scale. By evaluating these expressions we found that the anisoplanatic error increases as power-law exponent increases. We also found that the anisoplanatic error often saturates to a value less than 1 rad^2 after piston and tilt removal. Further, we found that as power law increases the contribution of piston and tilt dominate the anisoplanatic error expression. Relatedly, we saw that the magnitude of the outer scale contributes mostly to the piston and tilt terms. Together, we see that as power law increases and outer scale decreases it becomes less likely that anisoplanatism will affect the imaging system. This can be seen when for values of $D/r_0 < 10$, as L_0/D approaches unity, the anisoplanatic error saturates to a value less than 1 rad^2 even without piston or tilt removal. Under these conditions, the isoplanatic angle is effectively infinite and image reconstruction can succeed even though the field of view may be many times larger than the angular extent of the object. These results extend the assertion that the classic expression for the isoplanatic patch size is overly restrictive for cases when $D/r_0 < 10$, looking along horizontal paths in Kolmogorov turbulence. We also show that the isoplanatic patch size definition is overly restrictive in the same scenarios when non-Kolmogorov turbulence with $\alpha \geq 11/3$ is present. This may also apply in situations with a pronounced Hill bump

or where an inner scale term dominates. Lastly, these results also serve as an explanation for the observed efficacy of post-processing image reconstruction algorithms in horizontal imaging. We see that the removal of piston and tilt, along with the inclusion of a finite outer scale cause the isoplanatic angle to be much greater than the angle predicted by classical theory. In some cases the anisoplanatism is strong enough that these factors lead to a saturation in the anisoplanatic error, meaning the isoplanatic angle may be effectively infinite. Common reconstruction techniques used in incoherent imaging, like MFBD or SI techniques using the bispectrum, are insensitive to piston or are immune to variations in global tilt. The forward model used to inform these techniques is limited by the isoplanatic angle. This work shows that their effectiveness over scenes larger than the isoplanatic patch size may be due to an incomplete definition of the isoplanatic angle for incoherent imaging, especially in the case where the anisoplanatic error saturates when a practical outer scale and piston and tilt removal are considered.

This work relies on the assumption of a constant turbulence strength along the path, where in a real life scenario the turbulence strength may be weighted along the path. In a future work we aim to extend these results to a slant-path imaging scenario near the ground, where there is a height dependent $C_n^2(z)$ profile and a changing power-law exponent. Another overlooked point is that for a daylight standoff imaging scenario at 1 km, we need to account for a spherical wavefront. This change is likely to cause an increased isoplanatic angle and therefore a decreased saturation of the anisoplanatic

error in all cases.

Chapter 3

Angular Anisoplanatism Over Horizontal and Slant Paths in Non-Kolmogorov Turbulence

3.1 Introduction

Imaging over long horizontal and slant paths in the atmosphere differs from astronomical imaging. While both scenarios involve imaging through turbulence and are subject to blurring and distortion, many of the assumptions applied to astronomical imaging do not apply to imaging over long horizontal and slant paths. A very

common assumption is that imaging always happens within the isoplanatic angle, defined as the greatest angle between a point reference and an imaging target such that the anisoplanatic error is equal to 1 rad^2. In situations common to horizontal and slant path imaging, the isoplanatic angle can regularly be on the order of, or smaller than, the diffraction-limit of the system. The forward model used to inform Adaptive Optics (AO) techniques and image recovery techniques like Speckle Imaging (SI)[30, 31, 32, 33], Multi-frame Blind Deconvolution (MFBD)[34, 35, 36, 37, 38], and Phase Diversity[39, 40, 41, 42] is limited by the isoplanatic angle. However, the performance of SI techniques over scenes larger than the isoplanatic angle was first noted by solar astronomers[44]. Since then these techniques have been successfully used over extents ranging from several to many times the isoplanatic angle[43, 45, 56]. In [43], Bos showed that these techniques can be utilized even when the isoplanatic angle is on the order of the diffraction-limited sampling rate of the system, when the integrated turbulence in terms of D/r_0, is small.

In previous works[1, 47, 57], we showed that the efficacy of these techniques may be due to an incomplete definition of the isoplanatic angle for incoherent horizontal imaging. Techniques like MFBD or SI techniques using the bispectrum are insensitive to piston or are immune to variations in global tilt. We found that with the removal of piston and tilt, along with the inclusion of a finite outer scale, L_0, the effective isoplanatic angle was often much greater than the angle predicted by theory. In some cases these factors lead to a saturation in the anisoplanatic error, meaning that

the isoplanatic angle may be effectively infinite. Further, we found that the power law exponent, α, affects the anisoplanatic error expression. As the non-Kolmogorov power-law exponent increases, the contributions due to piston and tilt dominate the anisoplanatic error expression.

In our previous work[1], we made two simplifying assumptions. First, the anisoplanatic error expressions we derived modelled the angularly separated wavefronts as plane waves of infinite extent. In a daylight standoff imaging scenario at several hundred meters to a few kilometers, this is an incomplete model. At these distances the wavefront is correctly modelled as a spherical wavefront with a non-zero radius of curvature. Second, we used a constant turbulence strength, C_n^2, along the path. For purely a purely horizontal path this is a fair assumption. But, for the same conditions C_n^2 will vary with height when imaging along a slant path. This height dependence leads to a scenario where turbulence strength is not constant and varies as a function of height along the path.

In this work we examine the effect on the anisoplanatic error of using a wavefront with non-zero curvature and realistic slanted-paths. First, the anisoplanatic error is compared using plane wave and spherical wave source models in Kolmogorov and non-Kolmogorov turbulence. We find that using a wavefront model with a non-zero radius of curvature leads to a larger effective isoplanatic angle in all cases. This increase in effective isoplanatic angle means that the effect of anisoplanatism on imaging

is less severe in a more physical spherical wavefront scenario. Next, we compare a purely horizontal imaging scenario to a downward-looking and upward-looking slant-path imaging scenarios to investigate the effect that path-weighting plays on the saturation behaviour of the total, piston-removed, and piston-and-tilt-removed anisoplanatic error. We show that, compared to horizontal cases, upward looking cases were less affected by anisoplanatism and downward-looking cases were more affected. We also show that as the strength of the turbulence profile increases, the isoplanatic angle decreases for all cases. Additionally, as the strength of the C_n^2 profile increases, the isoplanatic angle decreases and the system is more likely to be affected by anisoplanatism.

The remainder of this work is outlined as follows. In the next section we present expressions for anisoplanatic error in non-Kolmogorov turbulence for a spherical wave model and a slanted-path respectively. The first expression in each is the total anisoplanatic error in non-Kolmogorov turbulence with a finite outer scale. The other two expressions are the anisoplanatic error due to piston and tilt. In Section 3.3.1 we evaluate the effects of power law, finite outer scale, and changing D/r_0 on the total, piston-removed, and piston-and tilt removed anisoplanatic error over a purely horizontal path for spherical and plane wave source models. In Section 3.3.2 we evaluate the effects of power law, finite outer scale, and a path dependent C_n^2 profile on the total, piston-removed, and piston-and-tilt-removed anisoplanatic error. Conclusions are provided in Section 3.4.

3.2 Background

In this section we provide the necessary expressions for total, piston-removed, and piston-and-tilt-removed anisoplanatic error between two wavefronts as they propagate over horizontal and slanted paths.

3.2.1 Horizontal path with a spherical wave model

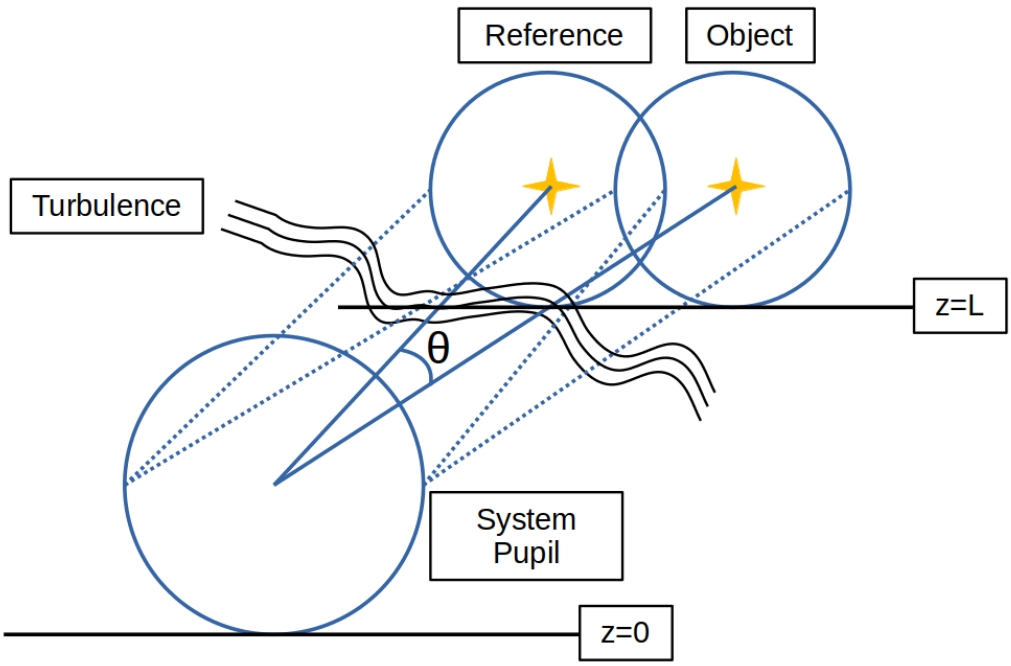

Figure 3.1: Horizontal propagation geometry. Two wavefronts, the reference and the object, are angularly separated. The angular separation leads to differing paths traveled by each wavefront, degrading the performance of phase correction.

Angular anisoplanatic error, when imaging along a purely horizontal path, can be modeled as two angularly separated wavefronts traversing a path from an imaging system at 0 to a target at a distance L, seen in Fig. 3.1. The two beams are angularly separated by θ, which leads to different turbulence-induced wavefront distortions for each wavefront. Here, the isoplanatic angle is the largest angular separation between identical points on each wavefront such that the anisoplanatic error is equal to 1 rad^2. As the angular separation increases, the correlation between the two wavefronts decreases. When the anisoplanatic error is greater than 1 rad^2, the wavefront correlation is so different that the atmospheric distortions become independent across the scene.

In a previous work[1] we derived an expression for the total differential phase variance between two plane waves as they propagate over a horizontal path as [1, Eq. 12,]. In this paper we are interested in investigating the effect of modelling the propagating wavefronts as spherical waves instead of plane waves. By changing the propagation parameter used previously to one for a spherical wave and following the same procedure, we arrive at

$$\begin{aligned}\sigma_{\phi}^{2}(\theta,\alpha) &= 4B(\alpha)c_1(\alpha)\int_0^L \mathrm{d}z\frac{\hat{r}_0(\alpha)^{2-\alpha}}{L} \\ &\times \int_0^\infty \mathrm{d}\kappa\kappa f(\kappa,\alpha)\left(1-J_0\left(\kappa\theta\left(z-z^2/L\right)\right)\right).\end{aligned} \tag{3.1}$$

Equation (3.1) is the total anisoplanatic error between two spherical waves propagating through a turbulent volume of depth L with an arbitrary power law exponent α. $\hat{r}_0(\alpha)$ is the generalized characteristic length, $B(\alpha) = \Gamma\left[\alpha/2\right] / \left(2^{2-\alpha}\pi\alpha\Gamma\left[-\alpha/2\right]\right)$ is a parameter that maintains consistency between the structure function and PSD descriptions of refractive index fluctuations, and $c_1(\alpha)$ is a constant equal to the value of the plane wave, wave structure function (WSF) at a separation equal to the characteristic length, $\hat{r}_0$ as described by Stribling [29]. Equation (3.1) includes the effect of piston and global tilt. Using the filter function expressions for piston [50], the phase variance due to piston is found to be

$$\begin{aligned}\sigma^2_{\phi,P}\left(\theta,\alpha\right) = 4B(\alpha)c_1(\alpha)\int_0^L \mathrm{d}z\frac{\hat{r}_0(\alpha)^{2-\alpha}}{L}\int_0^\infty \mathrm{d}\kappa\kappa f\left(\kappa,\alpha\right) \\ \times\left(1 - J_0\left(\kappa\theta\left(z - z^2/L\right)\right)\right)\left[\frac{2J_1\left(\kappa D/2\right)}{\kappa D/2}\right]^2.\end{aligned} \tag{3.2}$$

Lastly, the expression for the phase variance due to tilt is.

$$\begin{aligned}\sigma^2_{\phi,T}\left(\theta,\alpha\right) = 4B(\alpha)c_1(\alpha)\int_0^L \mathrm{d}z\frac{\hat{r}_0(\alpha)^{2-\alpha}}{L}\int_0^\infty \mathrm{d}\kappa\kappa f\left(\kappa,\alpha\right) \\ \times\left(1 - J_0\left(\kappa\theta\left(z - z^2/L\right)\right)\right) \\ \times\left(1 - \left[\frac{2J_1\left(\kappa D/2\right)}{\kappa D/2}\right]^2 - \left[\frac{4J_2\left(\kappa D/2\right)}{\kappa D/2}\right]^2\right).\end{aligned} \tag{3.3}$$

To get the phase variance due to the *removal* of piston and/or tilt Eqs. (3.2) and/or (3.3) are subtracted from Eq. (3.1). In Section 3.3.1 we compare the use of the above spherical wave expressions with corresponding plane wave expressions. The plane

wave expressions differ only in the content of the J_0 functions in Eqs. (3.1), (3.2), and (3.3). Full versions of the plane wave expressions and their derivations can be found in [1].

3.2.2 Slanted-path with a plane wave model

When looking at slanted-paths, we chose to investigate three geometries: an upward-looking, a downward-looking, and a purely horizontal case, all seen in Fig. 3.2. The purely horizontal scenario function as a baseline case to compare the behavior of the upward and downward-looking slanted path scenarios. In both slant path cases the imaging system and the target are horizontally separated by $\sqrt{L^2/2}$ m. In the upward-looking case, the imaging system is at ground level, $h = 0$ m, and the target is at $h = \sqrt{L^2/2}$ m in elevation. In the downward-looking case the imaging system is at $h = \sqrt{L^2/2}$ m and the target is at $h = 0$ m. From Fig. 3.2 it can be seen that the vertical and horizontal separations in each case were chosen such that the path actually traversed by the wavefronts is always L m for all three geometries.

Previously, we presented a derivation for the total, piston-removed, and piston-and-tilt-removed anisoplanatic error in the case of two horizontally propagating plane waves in [1]. These expressions allow for a height dependent turbulence strength

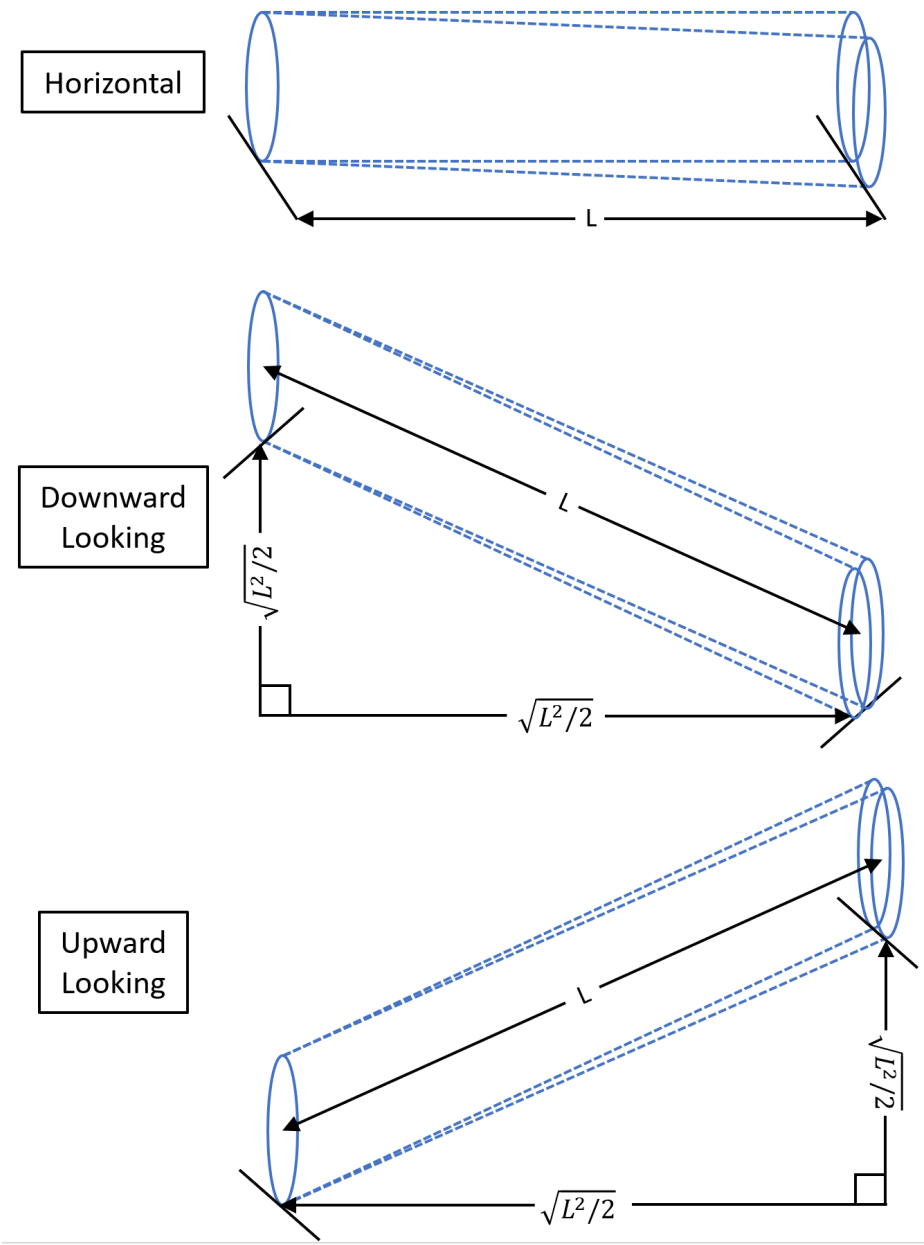

Figure 3.2: Horizontal and slanted propagation geometry for each of the scenarios examined in Section 3.3.2

profile, $C_n^2(z)$ and can be leveraged again in this work. We provide only the final expressions here. First, the expression for the total anisoplanatic error for two angularly

separated plane waves, including the effect of piston and global tilt,

$$\sigma^2_{\phi,P}(\theta,\alpha) = 4B(\alpha)c_1(\alpha)\int_0^L \mathrm{d}z \frac{\hat{r}_0(\alpha)^{2-\alpha}}{L}\int_0^\infty \mathrm{d}\kappa\kappa f(\kappa,\alpha) \times (1 - J_0(\kappa\theta z)). \tag{3.4}$$

Equation (3.4) is identical to [1, Eq. 12,]. Here the generalized characteristic length, $\hat{r}_0(\alpha)$ is derived from the power law exponent and the appropriate $C_n^2(z)$ profile for a given power law exponent and scene geometry. Similarly, the expression for the phase variance due to piston is

$$\sigma^2_{\phi,P}(\theta,\alpha) = 4B(\alpha)c_1(\alpha)\int_0^L \mathrm{d}z \frac{\hat{r}_0(\alpha)^{2-\alpha}}{L}\int_0^\infty \mathrm{d}\kappa\kappa f(\kappa,\alpha) \times (1 - J_0(\kappa\theta z))\left[\frac{2J_1(\kappa D/2)}{\kappa D/2}\right]^2, \tag{3.5}$$

and the expression for the phase variance due to tilt is

$$\sigma^2_{\phi,T}(\theta,\alpha) = 4B(\alpha)c_1(\alpha)\int_0^L \mathrm{d}z \frac{\hat{r}_0(\alpha)^{2-\alpha}}{L}\int_0^\infty \mathrm{d}\kappa\kappa f(\kappa,\alpha) \times (1 - J_0(\kappa\theta z)) \times \left(1 - \left[\frac{2J_1(\kappa D/2)}{\kappa D/2}\right]^2 - \left[\frac{4J_2(\kappa D/2)}{\kappa D/2}\right]^2\right). \tag{3.6}$$

Using Mellin transform techniques, we previously derived analytical expressions for Eqs. (3.4), (3.5), and (3.6) in the appendices of [1].

3.3 Results

3.3.1 Effect of spherical wave modelling on anisoplanatic error saturation

In this section we explore the effect of a change in power-law exponent, the inclusion of a finite outer scale, and a changing turbulence strength via $D/\hat{r}_0$ on the total, piston-removed, and piston-and-tilt-removed anisoplanatic error for two pairs of wavefronts propagating along the same horizontal path. One pair are modelled as plane waves and the other are modelled as spherical waves. In both cases the imaging system and the target are horizontally separated by $L = 1$ km.

First, we investigate the behavior of the ansioplanatic error when using a plane wave model or and a spherical wave model for a simple case. For the spherical wave model, Eqns (3.1), (3.2), and (3.3) are evaluated in terms of separation angle θ, for $D/\hat{r}_0 = 1$, 3, and 9, $L_0 = \infty$, and $\alpha = 11/3$. Similarly, expressions for the plane wave anisoplanatic error derived in [1] are evaluated over the same parameters and the results for both can be seen in Table 3.1. Bold values denote when the anisoplanatic error never reaches a value of 1 rad^2 and instead saturates and approaches some asymptotic value. In this case, the bold value is the angle at which the anisoplanatic

error is equal to $\left(1-\frac{1}{e}\right) \times$ *asymptotic value*. To avoid confusion, we refer to this angle as the *asymptotic isoplanatic angle* for the remainder of the paper. The ansioplanatic error for all the cases in Table 3.1 is plotted in Fig. 3.3, where solid lines represent the plane wave cases and dashed lines are the corresponding spherical wave cases.

		$D/\hat{r}_0$		
		1	3	9
Plane Wave	Total	62.49	20.82	6.90
	Total-P	**60.76**	44.74	9.85
	Total-P-T	**24.16**	**24.16**	11.66
Spherical Wave	Total	350.97	116.98	38.99
	Total-P	**285.28**	275.44	57.04
	Total-P-T	**140.00**	**140.00**	69.45

Table 3.1
Isoplanatic angles, in μradians, for plane and spherical wavefront models. These results include the total, piston removed, and piston and tilt removed isoplanatic angle for $D/\hat{r}_0 = 1$, 3, and 9, and all cases have a $\alpha = 11/3$ Kolmogorov power law exponent. Bold values indicate cases where the anisoplanatic error never reaches 1 rad^2 and instead saturates to an indicated *asymptotic isoplanatic angle*.

From Toselli et. al[58] we can relate the plane wave and spherical wave $\hat{r}_0$, as

$$\frac{r_{0,spherical}}{r_{0,plane}} = (\alpha - 1)^{\frac{1}{\alpha-2}} \tag{3.7}$$

If $\alpha = 3.1, 3.66$, and 3.9 are substituted into Eqn. (3.7) we get values of 1.96, 1.80, and 1.75 for power law exponents 3.1, 3.66, and 3.9 respectively. If we use these ratios as proportional estimates for change in isoplanatic angle, we expect the spherical wave isoplanatic angles to be 1.96 to 1.75 times the plane wave values, depending upon the value of α. However, from Table 3.1 we see that for all parameters, the isoplanatic

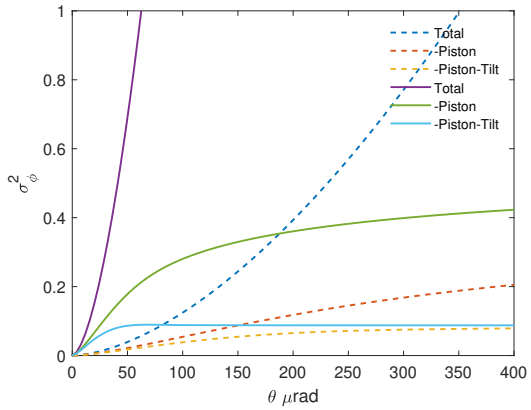

(a)

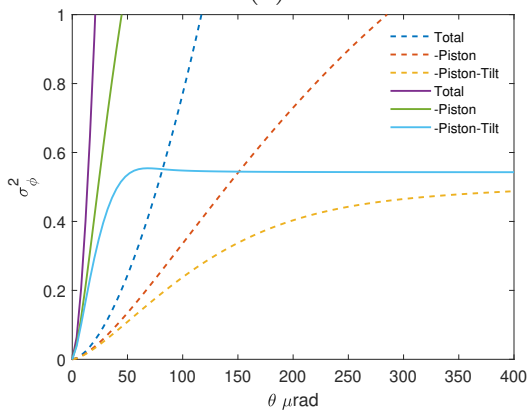

(b)

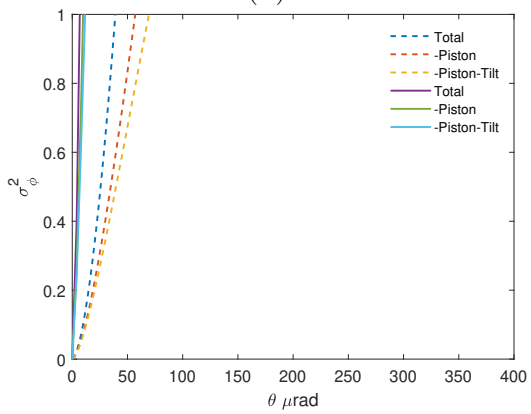

(c)

Figure 3.3: Anisoplanatic error as a function of θ for a fixed aperture size $D = 0.10$ m and values of $D/\hat{r_0} = 1, 3$, and 9 in subfigures **(a)** , **(b)**, and **(c)** respectively, along a horizontal path. An infinite outer scale and a power law exponent of $\alpha = 11/3$ is used for all cases. **Solid lines** denote a plane wave source model and **dashed lines** denote corresponding spherical wave source models.

angle is 5 to 7 times *larger* in the spherical wave case than its matching plane wave case when $\alpha = 3.66$. The removal of piston or piston and tilt increases the difference between the spherical and plane wave isoplanatic errors.

Now we look at the effect of a finite outer scale, L_0, and a changing power law exponent, α on the anisoplanatic error. We evaluate Eqns. (3.1), (3.2), and (3.3) for three values of $\alpha = 3.1$, 3.66, and 3.9 and for four outer scale values of $L_0/D = 1/3$, 1, 10, and ∞, seen in Table 3.2.

Looking at Table 3.2 we see several behaviors. First, the anisoplanatic error is more likely to saturate as $L_0/D \to 1$ and $D/\hat{r}_0 \to 1$. Second, as α increases the isoplanatic angle and asymptotic isoplanatic angle increase as well. Lastly, the removal of piston or piston and tilt causes an increase in isoplanatic angle and a decrease in asymptotic isoplanatic angle. These behaviors are consistent with our previous work when a plane wave source model was used [1].

There is one primary difference between the spherical and plane wave cases. The magnitude difference between plane wave and spherical wave isoplanatic angle observed in Table 3.1 is consistent for all values of α, when $L_0/D = \infty$. The spherical wave isoplanatic angle is consistently 5 to 7 times larger than the corresponding plane wave case. Much work is concerned about the limit imposed on imaging reconstruction and AO by the isoplanatic angle. From Table 3.2 we can see that this limit is significantly less severe if we include the effects of piston and/or global tilt removal, a finite outer

		D/r_0											
		$L_0/D = 1/3$			$L_0/D = 1$			$L_0/D = 10$			$L_0/D = \infty$		
		1	3	9	1	3	9	1	3	9	1	3	9
$\alpha = 3.1$	Total	**36.28**	**36.28**	**36.28**	**97.83**	**97.83**	53.7	463.67	125.43	39.33	342.49	114.16	38.05
	Total-P	**35.55**	**35.55**	**35.55**	**85.52**	**85.52**	54.36	**219.65**	161.05	41.85	**207.42**	156.83	41.61
	Total-P-T	**33.65**	**33.65**	**33.65**	**68.07**	**68.07**	56.60	**106.46**	337.17	45.21	**105.28**	327.88	45.08
$\alpha = 3.66$	Total	**48.26**	**48.26**	**48.26**	**127.47**	**127.47**	100.67	811.47	172.73	48.85	350.97	116.98	38.99
	Total-P	**47.05**	**47.05**	**47.05**	**109.90**	**109.90**	105.16	**294.70**	294.56	58.02	**285.28**	275.44	57.04
	Total-P-T	**43.91**	**43.91**	**43.91**	**85.97**	**85.97**	124.06	**139.76**	**139.76**	69.94	**140.00**	**140.00**	69.45
$\alpha = 3.9$	Total	**51.50**	**51.50**	**51.50**	**137.65**	**137.65**	**137.65**	2288.53	319.31	79.40	375.30	125.13	41.72
	Total-P	**50.36**	**50.36**	**50.36**	**118.21**	**118.21**	**118.21**	**357.77**	**357.77**	108.63	**315.45**	**315.45**	104.70
	Total-P-T	**47.20**	**47.20**	**47.20**	**91.99**	**91.99**	**91.99**	**156.25**	**156.25**	177.63	**154.79**	**154.79**	172.99

Table 3.2

Isoplanatic angles, in μradians, for varying power law, D/r_0, and L_0/D values. These results include the total isoplanatic angle, the piston-removed isoplanatic angle, and the piston and tilt removed isoplanatic angle for all cases of interest using the **spherical wave model**. Bold values indicate cases where the anisoplanatic error never reaches a value of 1 rad^2 and here it saturates to the specified asymptotic isoplanatic angle.

scale, and a more accurate spherical wave image formation model.

3.3.2 Evaluation of anisoplanatic error over slant paths

We now explore the effect of a change in power law, the inclusion of a finite outer scale, and increasing $C_n^2(z)$ profiles on the anisoplanatic error for the one-way *plane wave* case along two slant paths. We compare upward and downward-looking slant path geometries and an equivalent horizontal geometry for two turbulence profiles. In all three geometries, the path the wavefront traverses is $L = 1$ km. In both slant path cases the imaging system and the target are horizontally separated by $\sqrt{L^2/2}$ m. In the upward-looking case, the imaging system is at ground level, $h = 0$ m, and the target is at $h = \sqrt{L^2/2}$ m in elevation. In the downward-looking case the imaging system is at $h = \sqrt{L^2/2}$ m and the target is at $h = 0$ m. For all three geometries, the generalized characteristic length, $\hat{r}_0$ is derived from the power law exponent and the appropriate $C_n^2(z)$ profile for the given scene geometry. For the upward and downward-looking cases $\hat{r}_0$ is derived from a Hufnagel-Valley 5-7 [59] turbulence strength profile. In the horizontal case $\hat{r}_0$ is derived from a constant value of C_n^2, obtained from path averaging the upward and downward-looking $C_n^2(z)$ profiles. This approach is useful because it evenly distributes the turbulence along the horizontal path and weights the majority of the turbulence towards or away from the aperture for upward and downward-looking slant paths respectively.

Similarly to Section 3.3.1, values of α were chosen as $\alpha = 3.1$, $11/3$, and 3.9 and three outer scales of $L_0/D = \infty$, $L_0/D = 1$ and $L_0/D = \infty$ were investigated. We begin by evaluating Eqs. (3.4), (3.5), and (3.6) in terms of separation angle θ for the above parameters. The corresponding isoplanatic angle for each case can be seen in Table 3.3. We note that in some cases, denoted by a bold value, the anisoplanatic error never reaches a value of 1 rad^2 and so we list the *asymptotic isoplanatic angle*.

From Table 3.3 some behaviors emerge. When the total anisoplanatic error in the horizontal and upward-looking cases are compared, where turbulence is more strongly weighted closer to the aperture in the upward-looking case, the anisoplanatic error is reduced. In the purely infinite outer scale case, the isoplanatic angles are 2-4 times larger for the upward looking case than the horizontal case, for all power law exponents. With the removal of piston and tilt we see the same behavior when comparing the upward and horizontal cases for all values of α. In the upward-looking case the removal of piston and tilt is more likely to cause the anisoplanatic error to saturate to a value less than 1 rad^2 as α increases.

Similarly, when the horizontal and downward-looking cases are compared the same patterns emerge. Here the turbulence is more strongly weighted away from the aperture in the downward-looking case than the horizontal case. This leads to a 40-60% reduction in isoplanatic angle in the downward case compared to the horizontal cases and and a 10 times increase in the asymptotic isoplanatic error. When an infinite

		L_0/D								
		Horizontal			Upward			Downward		
		1	10	∞	1	10	∞	1	10	∞
$\alpha = 3.1$	Total	**43.69**	39.17	35.85	**234.75**	147.59	126.73	**22.24**	22.41	20.88
	Total-P	**35.51**	49.05	47.96	**194.55**	237.11	227.56	**18.76**	26.34	25.93
	Total-P-T	**27.90**	105.42	99.27	**155.18**	874.20	811.96	**15.25**	36.55	35.90
$\alpha = 3.66$	Total	**58.08**	49.81	34.46	**313.80**	167.01	101.13	**30.24**	30.09	21.62
	Total-P	**45.65**	80.83	75.51	**254.33**	400.53	348.37	**24.62**	43.56	41.62
	Total-P-T	**35.06**	**55.45**	**57.10**	**200.37**	**262.76**	**270.25**	**19.63**	**29.87**	**30.45**
$\alpha = 3.9$	Total	**65.71**	72.37	31.20	**341.18**	242.04	85.15	**33.27**	44.06	19.98
	Total-P	**50.05**	197.30	152.67	**274.50**	1218.54	752.66	**26.60**	90.05	77.99
	Total-P-T	**37.98**	**63.75**	**63.85**	**215.43**	**285.68**	**295.28**	**21.12**	**33.00**	**34.19**

Table 3.3

Isoplanatic angles, in μradians, for varying power law and L_0/D values for horizontal, upward-looking and downward-looking scenarios. These results include the total, piston-removed, and piston-and-tilt-removed isoplanatic angle for all cases of interest using the **plane wave model**. A bold value denotes a case where the anisoplanatic error never reaches a value of 1 rad^2 and here the *asymptotic isoplanatic angle* is listed.

outer scale is used, anisoplanatism has the greatest effect on the downward-looking case and the least effect on the upward-looking case with the horizontal case in between.

Looking again at Table 3.3, but to the cases with a finite outer scale of $L_0/D = 10$ or $L_0/D = 1$, we observe similar behavior to the infinite outer scale case. As L_0/D approaches unity, the anisoplanatic error saturates to a value < 1 rad^2 for all values of α and all geometries. However when we compare this to cases when $L_0/D = 10$ and $L_0/D = \infty$ we see that the removal of piston and tilt play the largest role. When piston and tilt are removed, the anisoplanatic error saturates for all outer scales, in all geometries, when $\alpha \geq 11/3$. This is because increasing α increases the relative energy in the piston and tilt terms. The fact remains that the piston and tilt components dominate the anisoplanatic error expression.

While the HV 5-7 profile is used because of its relatively strong turbulence near the ground, strongly anisoplanatic environments often have more severe $C_n^2(z)$ profiles. To investigate the impact of stronger $C_n^2(z)$ profiles on anisoplanatic error saturation behavior, the evaluation in Table 3.3 was repeated in Table 3.4. The characteristic length profiles $\hat{r}_0(\alpha)$ for each power law exponent and scene geometry were doubled. The results of the doubled profiles can be seen in Table 3.4.

When Table 3.4 is compared to Table 3.3 several behaviors emerge. In the cases where the anisoplanatic error doesn't saturate for both scenarios, as the turbulence strength

		L_0/D								
		Horizontal			Upward			Downward		
		1	10	∞	1	10	∞	1	10	∞
$\alpha = 3.1$	Total	34.96	20.31	19.34	67.33	71.63	65.63	17.33	11.61	11.15
	Total-P	36.20	22.41	22.20	88.54	87.97	86.31	17.64	12.53	12.44
	Total-P-T	41.69	25.77	25.64	122.71	120.86	119.61	18.94	13.80	13.77
$\alpha = 3.66$	Total	**58.86**	30.94	23.00	**363.24**	96.70	64.81	**30.32**	18.69	14.25
	Total-P	**46.27**	41.15	39.86	**223.74**	161.03	150.84	**24.73**	23.67	23.08
	Total-P-T	**35.53**	71.34	69.11	**182.93**	466.25	438.59	**19.72**	33.27	32.84
$\alpha = 3.9$	Total	**66.59**	46.06	21.91	**391.62**	141.80	57.50	**33.23**	28.11	13.92
	Total-P	**50.73**	76.69	71.09	**239.89**	342.50	290.61	**26.72**	42.42	40.15
	Total-P-T	**38.49**	**60.58**	**64.71**	**195.77**	**280.48**	**287.30**	**21.22**	**33.08**	**34.35**

Table 3.4

Isoplanatic angles in μradians, for the same parameters as in Table 3.3.
Here all turbulence strength profiles were doubled.

profile increases the isoplanatic angle becomes smaller. The effect of increasing $\hat{r}_0$ however becomes most apparent when looking at the cases where the anisoplanatic error saturates in Table 3.3. The anisoplanatic error is most likely to saturate in two cases. First, as $L_0/D \to 1$ for all values of α. Second, the removal of piston and tilt is likely to make the anisoplanatic error saturate for $L_0/D \geq 10$ for all geometries, when $\alpha \geq 3.66$. When the turbulence strength profile is doubled, in Table 3.4, we see that the anisoplanatic error no longer saturates when $L_0/D = 1$ in the cases where $\alpha = 3.1$ for upward, downward, or horizontal-looking geometries. Additionally the removal of piston and tilt only lead to anisoplanatic error saturation when $\alpha = 3.9$. As $\hat{r}_0$ increases, anisoplanatism is more likely to affect the system, for all outer scales and power law exponents.

3.4 Conclusion

In this paper we evaluated expressions for the total, piston-removed, and piston-and-tilt-removed anisoplanatic error for three different scene geometries and plane and spherical models.

The total, piston-removed, and piston-and-tilt-removed anisoplanatic error for varying power law exponent, $D/\hat{r}_0$, and L_0/D for a plane wave and a spherical wave model were compared. We observed that the spherical wave isoplanatic angle was larger than

its plane wave counterpart in all cases where the anisoplanatic error didn't saturate. In cases where the anisoplanatic error saturated, the *asymptotic isoplanatic angle* increased for all cases when a wavefront with a non-zero radius of curvature was used. The increase in actual and asymptotic isoplanatic angle for the sphere wave cases shows the necessity of using a spherical wave source model when trying to determine the effective isoplanatic patch size for a realistic horizontal imaging scenario.

The anisoplanatic error for an upward-looking and a downward-looking slanted-path were modelled and compared to a comparable horizontal path. Upward looking slant-path cases were less affected by anisoplanatism than a comparable horizontal scenario regardless of piston and tilt removal, outer scale size, or power-law exponent. Conversely, downward looking slant-path cases were more affected by anisoplanatism than a comparable horizontal scenario. Together, we saw that as turbulence was more strongly weighted near the aperture, both the isoplanatic angle and the asymptotic isoplanatic angle increased. In the presence of a finite outer scale the ansioplanatic error was more likely to saturate as $L_0/D \to 1$ regardless of piston and tilt removal or power-law exponent. Lastly, as the turbulence strength profile increased, the isoplanatic angle became smaller and the anisoplanatic error is less likely to saturate when $\alpha \leq 11/3$ for all outer scales, even with piston and tilt removal.

Much work is concerned with the limit imposed on imaging reconstruction and AO by the isoplanatic angle. The motivation of this work, and our previous work, was to

explore the effect of many different factors on the practical anisoplanatic error and effective isoplanatic angle for realistic horizontal imaging scenarios. When imaging over long horizontal and slant paths, where the isoplanatic angle is small and anisoplanatism dominates we see that this limit is significantly less severe than predicted. The limit imposed on the system by the anisoplanatic error is much less severe than predicted by classical isoplanatic angle expression, but only if we include the interplay of piston and/or global tilt removal, a finite outer scale, accurate image formation models, and realistic turbulence profiles.

This work demonstrates many scenarios where the anisoplanatic error theoretically saturates and the isoplanatic angle is effectively infinite. In practice there is likely an angular separation at which techniques, that are limited by the isoplanatic angle, are likely to break down. In future work we aim to evaluate common techniques like SI or MFBD in situations where we find that the anisoplanatic error saturates.

Chapter 4

Working Title: Effect of Finite Inner Scale on the Saturation Behavior of Branch-Point Density

4.1 Introduction

The branch-point problem is a multifaceted problem that ultimately degrades one's ability to perform phase compensation. In turn, researchers need to study all aspects of the problem to quantify its limitations. This chapter, as a result, uses wave-optics simulations to study the branch-point problem in earnest.

The presence of distributed-volume atmospheric aberrations (aka deep turbulence) presents unique challenges for beam-control applications, which look to sense and correct for disturbances found along the laser-propagation path. In practice, deep-turbulence conditions result in a phenomena known as scintillation (i.e., the constructive and destructive interference that manifests from coherent-light propagation through distributed-volume atmospheric aberrations). The Rytov number, also referred to as the log-amplitude variance, gives a a gauge for the strength of the scintillation experienced. As the scintillation becomes severe (e.g., for Rytov numbers greater than 0.1), total-destructive interference gives rise to branch points in the phase function; in particular, at points where the real and imaginary parts of the complex-optical field equate to zero.

Branch points, at large, add a rotational component to the phase function that traditional-least-squares phase reconstruction algorithms cannot account for. As such, one often refers to the rotational component as the hidden phase, thanks to the foundational work of Fried [60]. The existence of branch points then leads to unavoidable 2π phase discontinuities in the phase function known as branch cuts.

These branch cuts, in practice, become linked to positively and negatively charged branch points. Because of inter-actuator coupling, continuous-face sheet deformable mirrors (DMs) with high-power coatings are unable to fully compensate for the branch cuts. Thus, in the presence of moderately deep turbulence, with Rytov numbers

greater than ≈ 0.5, the corresponding branch-point problem tends to be the "Achilles' heel" to current phase-compensation solutions [9].

In an effort to study the branch-point problem in earnest, this paper uses a metric referred to as the branch-point density (i.e., the number of branch points contained within the limiting aperture in a pupil plane). This metric is straightforward to compute using wave-optics simulations. Thus, our work studies the branch-point density as a function of the Rytov number, in addition to grid resolution and inner scale. To our knowledge, such a study has never been performed, and the results show that provided adequate grid resolution, the branch-point density grows without bound as the Rytov number increases. The results also show that this growth becomes limited with the presence of a finite inner scale. Such results will ultimately inform future phase-compensation research efforts, so that researchers can develop novel phase-compensation systems that sense and correct for the effects deep turbulence.

In what follows, Sec. 4.2 contains background material on the history of the branch-point problem. Section 4.3 explores the trade space, and the results and discussion follow in Sec. 4.4. We then provide a conclusion for this work in Sec. 4.5.

4.2 Background

Until the early 1970's there was a long history of studying phase, ϕ, distortions, where the phase is a single-valued function of coordinates. Nye and Berry[61], however proposed another type of phase distortion with singularities in the phase, which they called phase dislocations. These are known commonly by several names: phase dislocations, screw dislocations, optical vortices, and branch points. In this paper this phenomenon shall be referred to as branch points. Afterwards, many theoretical and experimental investigations[62, 63, 64, 65, 66, 67, 68, 69, 70, 71, 72, 73, 74, 75, 76] supporting the existence of branch points in optics were published. The primary characteristic of a branch point is the existence of points where the field of the gradient of phase becomes a vortex one, or mathematically $\nabla \times \nabla\phi = 0$. For this to occur, there must be a null in the wavefront amplitude, A, at this point.

Various applications of branch points in different areas of optics were then suggested. Among them, the concept of turbulence-induced branch-points was first proposed and proven by Fried and Vaughn[8]. When propagating light through a turbulent media, the wavefront passes through refractive-index inhomogeneities that cause amplitude and phase fluctuations at the observation plane. If the fluctuations are strong enough, constructive and destructive interference occurs during propagation and points of zero amplitude can form at the observation plane, leading to the creation of branch points

in the phase function. Fried and Vaughn carried out a numerical simulation for a laser beam propagating through Kolmogorov turbulence, which showed a number scenarios in which branch points can be seen within the wavefront. The authors also suggested a potential procedure of phase reconstruction in the presence of branch points, which inspires a number of works discussed later.

The problem of turbulence-induced branch points was also discussed by Tartakovski et al.[77], who analyzed the properties of the point-spread function (PSF) associated with branch points[78]. Lukin and Fortes[79, 80] investigated the effect of branch points on phase conjugation instability with thermal blooming compensation in Adaptive Optics (AO) systems.

Voitsekhovich et al.[15] were the first to investigate the density of branch point occurrence. The authors use numerical simulation and a theoretical treatment to provide an estimation of branch point density for various turbulence parameters. Various turbulence conditions, ranging from weak to strong scintillation, were considered as well as the dependence on wavelength and various inner scales of turbulence for a fixed grid resolution of 512×512. Voitsekhovich et al. identified *four* key regions where the branch point behavior differs. First, a region where the log-amplitude statistics are nearly Gaussian, associated with weak turbulence, where the branch point density is small. Second, a region between weak and strong turbulence where the branch point density grows rapidly. In the third region, where turbulence is strong the branch point

density is replaced by a slower but still nonlinear increase. Lastly, in the turbulence strength saturation regime, the branch point density increases linearly.

In 1998 Fried[60] demonstrated the issues with using the common Least Mean Square Error (LMSE) type of wave-front reconstructor to sense all of the turbulence-induced phase perturbations. Fried began by explaining that the gradient of phase measured by a sheering interferometer is not continuous. The measurement of the interferometer must therefore be represented as the sum of the gradient of a scalar potential and the curl of the gradient of some vector potential. This meant that a LMSE reconstruction algorithm would neglect part of the phase known as the "hidden phase." Leaving the hidden phase out means that the AO system would perform improper corrections. To explore this phenomenon, Fried made the case that branch points could be represented analytically. This was accomplished by starting with a contour integral around a point in the gradient of the phase function where the contour integral does not equal zero and instead equals $\pm 2\pi$. A hertz function could then be used to describe the hidden phase. From this derivation Fried made two key assertions. One, the density of branch points and the distance between branch point pairs both matter. This meant that a weaker scintillation, produced by distant turbulence, with a greater distance between positive and negative branch point pairs may pose a greater problem for AO performance than stronger scintillation, produced by stronger turbulence, at a shorter range where the branch point pairs are closer together. The second assertion was that by analytically defining the value of the hidden phase based on branch point

location, Fried set up a potential avenue to construct a branch point tolerant LMSE reconstructor.

After Fried's analytical characterization of branch points, work in the field can be loosely categorized into two groups. Work on branch point tolerant phase reconstruction methods and further characterization of the existence and behavior of branch points. With respect to the first category, there are many works[10, 11, 12, 13, 81, 82] that have attempted to provide branch point tolerant LMSE reconstruction algorithms with varying degrees of efficacy. Branchers et al. [9, 83] investigated the use of both Shack-Hartmann sensors and shearing interferometers in strong scintillation, where branch points are most likely to occur. They found, in the presence of branch points, the Shack-Hartmann sensor performed poorly and the shearing-interferometer performed much better. All branch point tolerant LMSE reconstructors rely on the ability to detect branch points from wavefront sensor measurements. Different strategies for detecting the location of branch points have been proposed by many authors. [84, 85, 86]

A more recent effort has been made to describe the evolution of what are called vortex beams in atmospheric optical turbulence. Vortex beams differ from imaging discussions of branch points in that there is only one phase singularity which circulates around an amplitude null centered within the laser beam and along the axis of propagation. The study of this phenomena is known as singular optics.[87] Vortex

beams have been investigated for use as information carriers in optical communication [88] and as optical tweezers and spanners. [89] These potentially useful applications are possible because vortex beams carry orbital angular momentum and topological charge through atmospheric turbulence.[90] When propagated through turbulence, work[91] has shown that while topological charge was conserved, which is useful for applications like optical communication, the scintillation characteristics of the beam were not as stable and were readily affected by atmospheric turbulence.

Most recently, work by members of the Starfire Air Force Research Laboratory has investigated the aggregate behavior of branch points. The aggregate behavior is examined in an attempt to relate branch points measured in the pupil to the upstream turbulence that created them. Sanchez and Oesch began by exploring the behavior of branch point density as a characteristic of an atmospheric turbulence simulator.[92] Here they showed that estimating the scintillation index for Rytov values above 0.4 does not provide accurate measurements for calibrating the atmospheric turbulence simulator. Due to branch points appearing at Rytov values greater than 0.1, they proposed that the density and distribution of branch points could be used to calibrate an atmospheric turbulence simulator. They found that the branch point density saturates for higher turbulence strengths and greater propagation distances, limiting its usefulness as a calibration metric. Next, Oesch et al. investigated the creation and evolution of branch points.[93] The authors mathematically proved that branch points must always form in positive and negative pairs and that these pairs occur in

a uniformly propagating wave in the atmosphere. They then used these results to show that once branch points are created in the atmosphere, they are persistent when uniformly propagated to a pupil. Due to branch points being uniformly persistent, the branch cut linking two points must evolve uniformly as well. This means that there is a smoothness to the mapping and that branch points must be a persistent feature of the propagating wave.[94] The postulate here and then later confirmed that atmospherically created branch point pairs separate as they propagate, and that they carry both the velocity of, and the distance to the turbulence layer that created them.[95, 96] This body of work culminated in a paper on characterizing the aggregate behavior of branch points in wave optics simulations.[97] Through independent wave optics simulation the authors demonstrated that the four properties of pupil plane branch points: motion, density, separation, and persistence provide a means to determine four terms for the layered atmospheric model: number, velocity, distance, and strength of the layers. By demonstrating this relationship, they are able to show that the four properties of branch points are actually properties of the travelling optical wave. Since this publication several works[98, 99] have posited that because branch-points are an enduring feature of the propagating wave they may also act as markers for photons with Orbital Angular Momentum (OAM) in the propagating beam.

Lastly, in biomedical optics speckle imaging techniques are often used to gain insight about the internal characteristics of tissue and biological fluid samples. These speckle

patterns are created by interference and, inherently, contain branch points. Recent works[100, 101] have demonstrated that the changing behavior of branch points could be used to determine the decorrelation behavior and scatterer dynamics in speckle-imaged tissue. It has also been shown that the through Poincare analysis, the behavior of branch points can be used to accurately estimate speckle sizes, even in cases with heavy speckle degradation.[102]

4.3 Simulation Setup and Exploration

The desired setup is as follows. We wish to propagate a plane wave with a wavelength of 1 μm along a propagation path with simulated deep turbulence. After propagation we wish to characterize the population of branch points in each scene. To this end, we briefly review the details associated with the necessary sampling and scene geometry, deep turbulence conditions, a short exploration of spurious branch points, and a characterization of the log-amplitude variance in deep turbulence.

4.3.1 Parameters of interest

To investigate and characterize branch-point density a testing scenario needs to be defined. For propagation, a plane wave source was chosen. A plane wave is the

simplest source model such that we can be sure that the target plane is illuminated, without worrying about effects like beam wander if a narrow Gaussian beam is used. Table 4.1 contains all the parameters of interest in the wave-optics simulations. It is important to note that the wave-optics simulations used $N \times N$ grids. The side length S was the same in both the source and target planes, allowing for unity scaling within the wave-optics simulations. The simulation also satisfied Fresnel scaling, such that $N = S^2/(\lambda Z)$, where λ is the wavelength and Z is the propagation distance. Satisfying this scaling determined the lowest resolution grid that could be used was 512×512. We also define a Guard Band Ratio (GBR) as $GBR = S/D$.

Table 4.1
Parameters of interest in the wave-optics simulations.

Parameters (MKS units)	Symbol	Value(s)
Grid	NxN	2^9 - 2^{14}
Side length (m)	S	1.6
Wavelength (m)	λ	1×10^{-6}
Propagation distance (m)	Z	5×10^{3}
Aperture diameter (m)	D	0.20
Guard Band Ratio	GBR	8

4.3.2 Deep turbulence conditions setup

While Table 4.1 contains all the parameters of interest in the wave-optics simulations, Table 4.2 makes use of several closed-form expressions to define the turbulence scenarios that make up the trade space. The primary characteristic used to define the turbulence scenarios in Table 4.2 is the plane-wave Rytov number, $\mathcal{R}_{PW}$. From the

Table 4.2
Some of the Turbulence scenarios used in the wave-optics simulations.

Scenario	$\mathcal{R}_{PW}$	C_n^2 ($\mathrm{m}^{-2/3}$)	$D/r_{0,PW}$	$\theta_0/(\lambda/D)$
1	0.1	6.31×10^{-16}	2.15	2.10
2	0.2	1.26×10^{-15}	3.26	1.38
3	0.3	1.89×10^{-15}	4.16	1.09
4	0.4	2.53×10^{-15}	4.94	0.91
5	0.5	3.16×10^{-15}	5.65	0.80
6	0.6	3.79×10^{-15}	6.30	0.72
7	0.7	4.42×10^{-15}	6.91	0.65
8	0.8	5.05×10^{-15}	7.48	0.60
9	0.9	5.68×10^{-15}	8.03	0.56
10	1.0	6.31×10^{-15}	8.56	0.53
20	2.0	1.26×10^{-14}	12.97	0.35
30	3.0	1.89×10^{-14}	16.54	0.27
40	4.0	2.53×10^{-14}	19.66	0.23
50	5.0	3.16×10^{-14}	22.47	0.20
60	6.0	3.79×10^{-14}	25.07	0.18
70	7.0	4.42×10^{-14}	27.50	0.16
80	8.0	5.05×10^{-14}	29.80	0.15
90	9.0	5.68×10^{-14}	31.98	0.14
100	10.0	6.31×10^{-14}	34.06	0.13

Rytov approximation, the propagation of a plane wave through turbulence has an associated path-integral expression that can be used as a metric for the amount of scintillation.[18, 50, 103] This value is known as the plane-wave Rytov number, $\mathcal{R}_{PW}$, also often labelled as the plane-wave log-amplitude variance. This path-integral expression is written as,

$$\mathcal{R}_{PW} = 0.563k^{7/6}\int_0^Z C_n^2(z)\,(Z-z)^{5/6}\,\mathrm{d}z, \tag{4.1}$$

where $k = 2\pi/\lambda$ is the angular wavenumber and $C_n^2(z)$ is the path-dependent refractive index structure coefficient. Given a propagation path with constant atmospheric

conditions, the path-integral expression can be reduced to the well known closed-form expression,

$$\mathcal{R}_{PW} = 0.307k^{7/6}C_n^2 Z^{11/6} \tag{4.2}$$

When $\mathcal{R}_{PW} = 0.1$ branch points begin appearing in the phase function[8, 60], thus the turbulence scenarios begin at this value and continue up to $\mathcal{R}_{PW} = 10.0$. For completeness in defining the turbulence scenarios, Table 4.2 also makes use of the plane-wave Fried parameter $r_{0,PW}$ (also known as the plane-wave coherence diameter or length):

$$r_{0,PW} = \left[0.423k^2 \int_0^Z C_n^2(z)\mathrm{d}z\right]^{-3/5}, \tag{4.3}$$

and the isoplanatic angle, θ_0:

$$\theta_0 = \left[2.91k^2 \int_0^Z C_n^2(z)\,(Z-z)^{5/3}\,\mathrm{d}z\right]^{-3/5} \rightarrow \theta_0 = 0.314\frac{r_{0,PW}}{Z}. \tag{4.4}$$

The turbulence scenarios in Table 4.2 are explored in Section 4.4 using both the well known idealized Kolmogorov power spectrum and the Hill power spectrum. In wave-optics work an idealized Kolmogorov spectrum with zero inner scale, $l_0 = 0$ m, and an infinite outer scale, $L_0 = \infty$ m is often used to reduce computation time and simplify complex integral expressions often found in imaging and beam control. However this is not an accurate representation of the energy distribution in a turbulent volume. This can be remedied by using a modified spectrum like the Hill or Von-Karman spectrum.

In this work the Hill spectrum is used, because it adds high spatial frequency content to the power spectrum description of the turbulence. Branch points arise due to scintillation such that using a spectrum that adds high spatial frequency content increases the scintillation and should therefore increase the number of branch points observed. We explore the effect of using a Hill spectrum in Section 4.4, where we use four inner scales: 3.1 mm, 6.2 mm, 12.4 mm, and 24.8 mm. These values were chosen because they represent inner scales equal to one, two, four, and eight grid points respectively.

4.3.3 Spurious branch point exploration

It is useful to define here, mathematically, what a branch point is and how it is detected. An arbitrary propagating optical wave U is represented as a phasor such that,

$$U = A \exp\left(-j\phi\right). \tag{4.5}$$

If the log amplitude variance σ_χ^2 is large enough, large amplitude fluctuations caused by atmospheric turbulence can result in total destructive interference, creating nulls in the irradiance. This null in irradiance causes a discontinuity in the phase function

$$\phi = \mathrm{Arg}(U) = \tan^{-1}\left[\frac{\mathrm{Im}(U)}{\mathrm{Re}(U)}\right], \tag{4.6}$$

known as a branch point, where $\mathrm{Re}(U)$ and $\mathrm{Im}(U)$ are the real and imaginary components of the optical disturbance U. When Eq. (4.5) is substituted into Eq. (4.6), the resulting value of ϕ is referred to as the wrapped phase. When the amplitude of the phasor is equal to zero, the argument is indeterminate and therefore a multi-valued function also known as a branch point.

To calculate the number of branch points in a given field we can use the following relationship,

$$\oint_C \nabla\phi\left(x, y, 0\right) \cdot \mathrm{d}\mathbf{r} = \pm 2\pi \left(N_+ - N_-\right), \tag{4.7}$$

where N_+ is the number of positive branch points and N_- is the number of negative branch points within the collimated phase function $\phi(x, y, 0)$. The relationship in Eq. (4.7) says that we can determine the location of a branch point when the line integral around the closed curve C of the gradient of the collimated phase function $\nabla\phi(x, y, 0)$ does not equal zero. More specifically, where $\nabla\phi(x, y, 0)$ is a non-conservative vector field. The sign of the closed-loop contour integration in the counter-clockwise direction determines the polarity of the branch points within Eq. (4.7). To implement this relationship numerically, WavePlex discretely samples the continuous integral in Eq. (4.7) by dividing the $N \times N$ grid into many 2×2 sub-grids and summing up the phase derivative around each point. A positive 2π value results in a positive branch point and a negative 2π value results in a negative branch point. Finally, to calculate the total number of branch points, the total number of positive and negative branch

points associated with the pixels found within $\phi(x, y, 0)$ is summed.

The method used by WavePlex to detect branch points at the grid level can often produce what are termed as spurious branch points. These are characterized as a pair (positive and negative) branch points which are centered on immediately adjacent grid points. To address this WavePlex has an algorithm that can be used to identify spurious branch points and remove them from the final count. The impact of these spurious branch points can be seen in Fig. 4.1. From **c** and **d** in Fig. 4.1 we can see that spurious branch points make up a significant portion of the branch points identified by WavePlex initially are spurious. In Section 4.4 we present results with spurious branch points included and removed.

From Fig. 4.1 we can see that spurious branch points make up a significant portion of the branch points identified by WavePlex initially are spurious. In Section 4.4 we present results with spurious branch points included and removed.

4.3.4 Log-amplitude variance exploration

With respect to scintillation, turbulence is often split into two regimes based upon the Rytov approximation. When the plane-wave Rytov number, $\mathcal{R}_{PW} < 0.25$, we call this the weak scintillation regime. Here, the Rytov number and the log-amplitude variance σ_χ^2 can be used interchangeably. In contrast, when the plane-wave Rytov number,

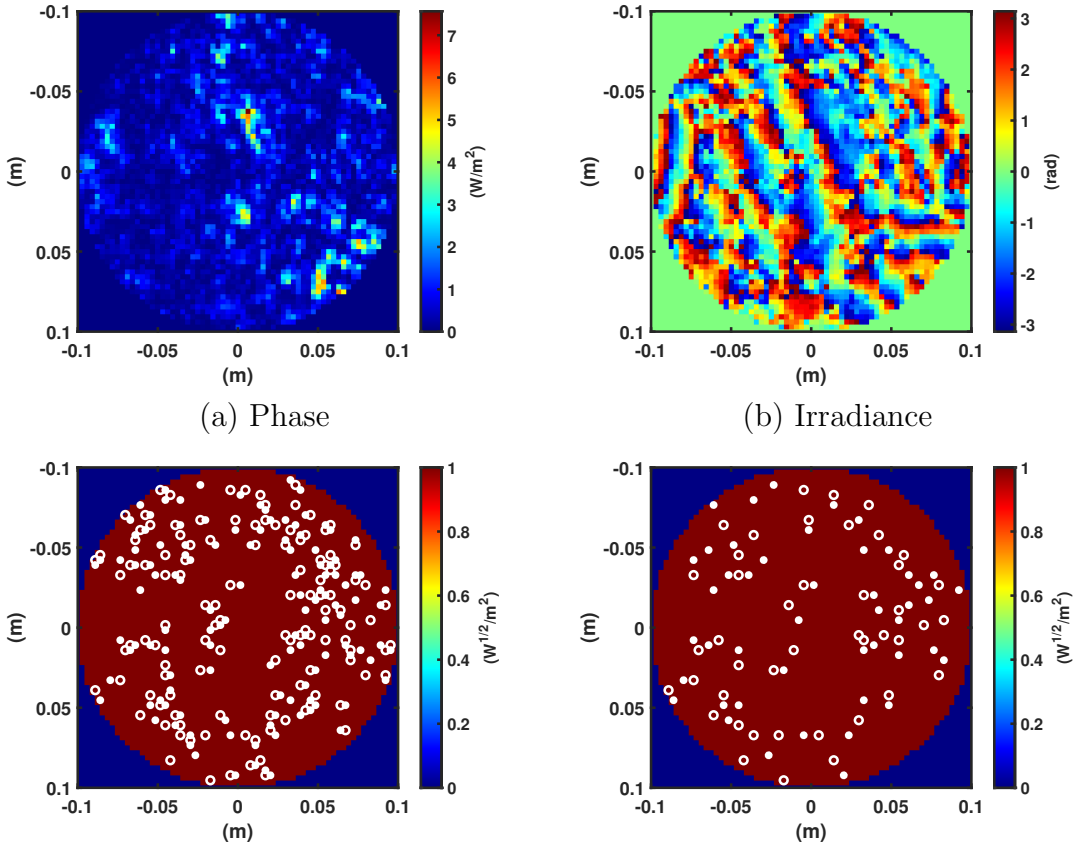

(a) Phase (b) Irradiance

(c) Total branch points (d) No spurious branch points

Figure 4.1: This figure provides a demonstration of WavePlex's branch point detection algorithm. **(a)** is the irradiance at the target plane of a plane wave after being propagated through ≈ 4 km of Kolmogorov turbulence, **(b)** is the associated phase at the target plane , **(c)** is the total number of branch points detected by WavePlex in the phase function, and **(d)** is the number of branch points in the target plane after removing spurious branch points.

$\mathcal{R}_{PW} \geq 0.25$, the Rytov approximation begins to break down in what is known as the strong scintillation regime. This behavior can be seen in Fig. 4.2, where the log-amplitude variance is numerically calculated as a function of the plane-wave Rytov variance for two different screen resolutions, $N = 512$ and $N = 16,384$. The black line denotes where $\sigma_\chi^2 = \mathcal{R}_{PW}$. For both resolution cases, the log-amplitude variance and the plane-wave Rytov number are almost identical up until around $\mathcal{R}_{PW} = 0.4$.

After that the log-amplitude variance begins to quickly saturate.

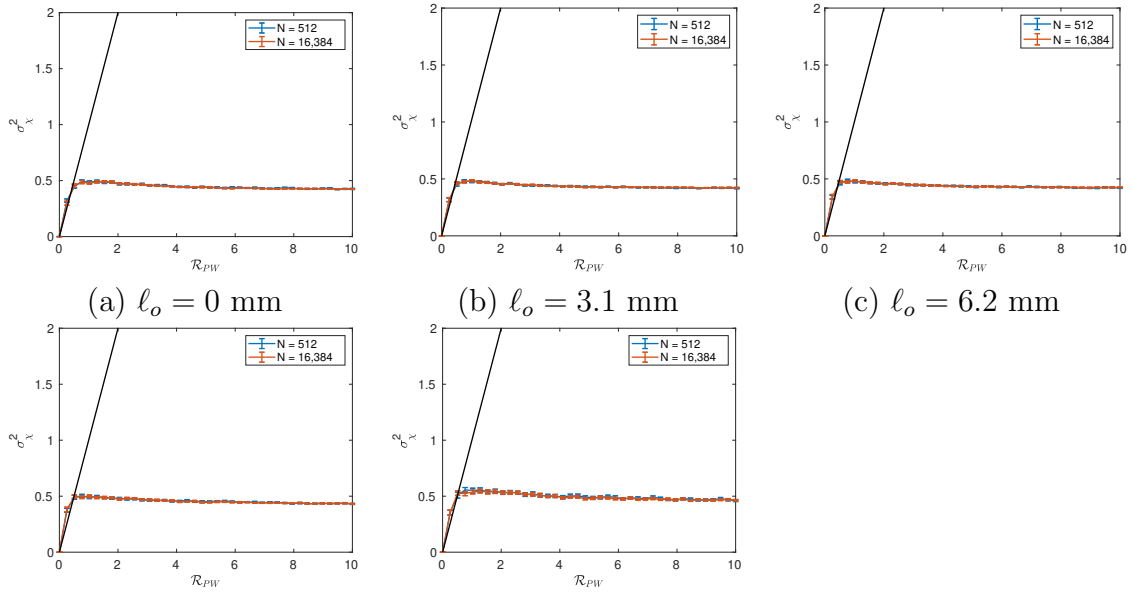

(a) $\ell_o = 0$ mm (b) $\ell_o = 3.1$ mm (c) $\ell_o = 6.2$ mm

(d) $\ell_o = 12.4$ mm (e) $\ell_o = 24.8$ mm

Figure 4.2: The Log-amplitude variance, σ_χ^2 as a function of the plane wave Rytov number, $\mathcal{R}_{PW}$, and the screen resolution, N. In each sub-figure a different inner scale, ℓ_o, value was used as follows: **(a)** Kolmogorov spectrum where $\ell_o = 0$ mm, **(b)** Hill spectrum where $\ell_o = 3.1$ mm, **(c)** $\ell_0 = 6.2$ mm, **(d)** $\ell_o = 12.4$ mm, and **(e)** $\ell_o = 24.8$ mm. Here the curves represent the averages and the error bars represent the standard deviations associated with 100 Monte Carlo realizations. Note that the solid black line in each sub-figure denotes where $\sigma_\chi^2 = \mathcal{R}_{PW}$.

In Fig. 4.2 **(b)** through **(e)** the same comparison between log-amplitude variance and plane-wave Rytov number is made, the only change is the use of a Hill spectrum with a practical inner scale of 3.1 mm through 24.8 mm. From these graphs we can see that the inclusion of a finite inner scale causes a difference in $\mathcal{R}_{PW}$ and σ_χ^2 even in the weak scintillation regime. However, with or without a finite inner scale, it is clear that there is a mismatch between $\mathcal{R}_{PW}$ and σ_χ^2, especially when $\mathcal{R}_{PW} \geq 0.4$. This mismatch indicates that if we want to investigate branch point density in the

deep turbulence regime, where $\mathcal{R}_{PW} \geq 1.0$, we cannot use σ_χ^2 to describe turbulence strength.

4.4 Results

In this section, we make use of the wave-optics simulations setup in Sec. 4.3 to explore the trade space. In particular, Fig. 4.3 shows the results for the *total* branch-point density, $\mathcal{D}_{BP}$, as a function of plane-wave Rytov number, $\mathcal{R}_{PW}$ and resolution N, for inner scale values of $\ell_0 = 0$, 3.1, 6.2, 12.4, and 24.8 mm. For reference, branch-point density is defined as $\mathcal{D}_{BP} = \frac{N_{BP}}{\pi(D/2)^2}$. We note that in Fig. 4.3 the curves report the averages and the error bars represent the standard deviations associated with 100 Monte Carlo realizations. Also note that the widths of the error bars are reasonably small and thus we believe that 100 Monte Carlo realizations are adequate in quantifying the behavior of $\mathcal{D}_{BP}$.

From Fig. 4.3, we can see that $\mathcal{D}_{BP}$ increases without bound as a function of both resolution and $\mathcal{R}_{PW}$ when $\ell_0 = 0$ mm. Relatedly in Fig. 4.3, graphs **(b)** through **(e)** show that when a finite inner scale is introduced the growth of $\mathcal{D}_{BP}$ as a function of $\mathcal{R}_{PW}$ decreases as the finite inner scale grows. As larger inner scales are introduced, such as in Fig. 4.3 **(d)** or **(e)**, $\mathcal{D}_{BP}$ for resolutions greater than $N = 512$ saturate closer and closer to $N = 512$. This means that when modelling the behavior of branch

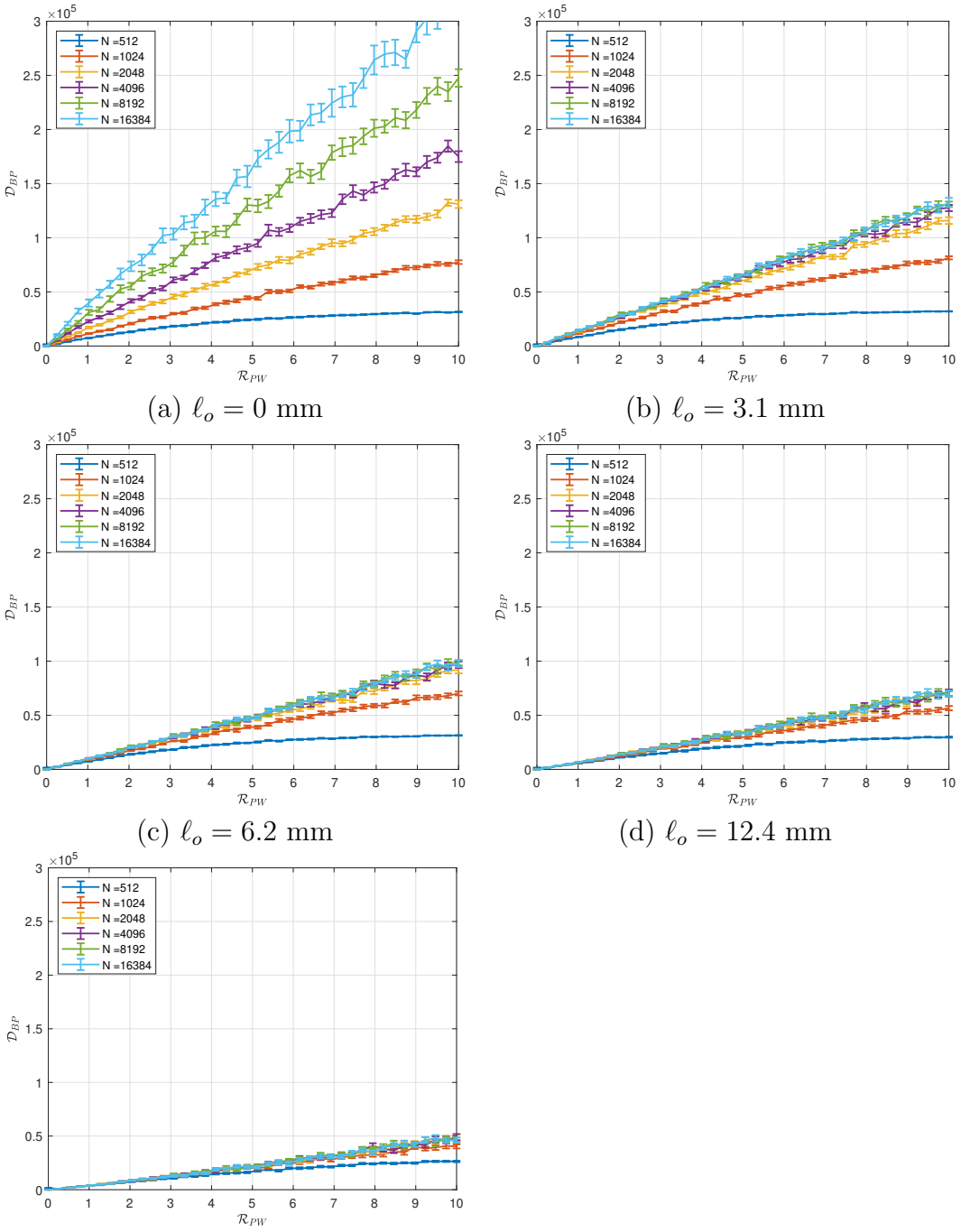

(a) $\ell_o = 0$ mm

(b) $\ell_o = 3.1$ mm

(c) $\ell_o = 6.2$ mm

(d) $\ell_o = 12.4$ mm

(e) $\ell_o = 24.8$ mm

Figure 4.3: Total branch point density as a function of spherical-wave Rytov number, $\mathcal{R}_{PW}$ for grid resolutions $N = 512$, 1024, 2048, 4096, 8192, and 16,384. In each sub-figure a different inner scale was used such that, **a** Kolmogorov power spectrum with $l_0 = 0$ mm, **(b)** Hill spectrum with $l_0 = 3.1$ mm, **(c)** $l_0 = 6.2$ mm, **(d)** $l_0 = 12.4$ mm, and **(e)** $l_0 = 24.8$ mm.

points in a wave-optics simulation, a mismatch in $\mathcal{D}_{BP}$ for different values of N may indicate that the simulation is being undersampled.

Figure 4.4 are the same simulation results found in Fig. 4.3, except the spurious branch-points have been removed using WavePlex's circulations function. If we compare the $\ell_0 = 0$ mm case in Figs. 4.3 and 4.4, we see that the removal of spurious branch points causes $\mathcal{D}_{BP}$ to begin saturating for $N = 512$ and $N = 1024$. Comparing Figs. 4.3 and 4.4 we see that the inclusion of finite inner scale causes the growth of $\mathcal{D}_{BP}$ as a function of $\mathcal{R}_{PW}$ to decrease, but not saturate, regardless of spurious branch point removal.

4.5 Conclusions

In this paper we used wave-optics simulations to look at the effect of finite inner scale and grid resolution on branch-point density in deep turbulence. Overall the results showed that increasing grid resolution and plane-wave Rytov variance cause the branch-point density to increase without bound if an ideal, 0 mm inner scale is used. When a non-zero inner scale is used, via a hill spectrum, the growth of the branch-point density as a function of Rytov number is significantly reduced.

Looking to the future, an expanded investigation of branch-point density may be

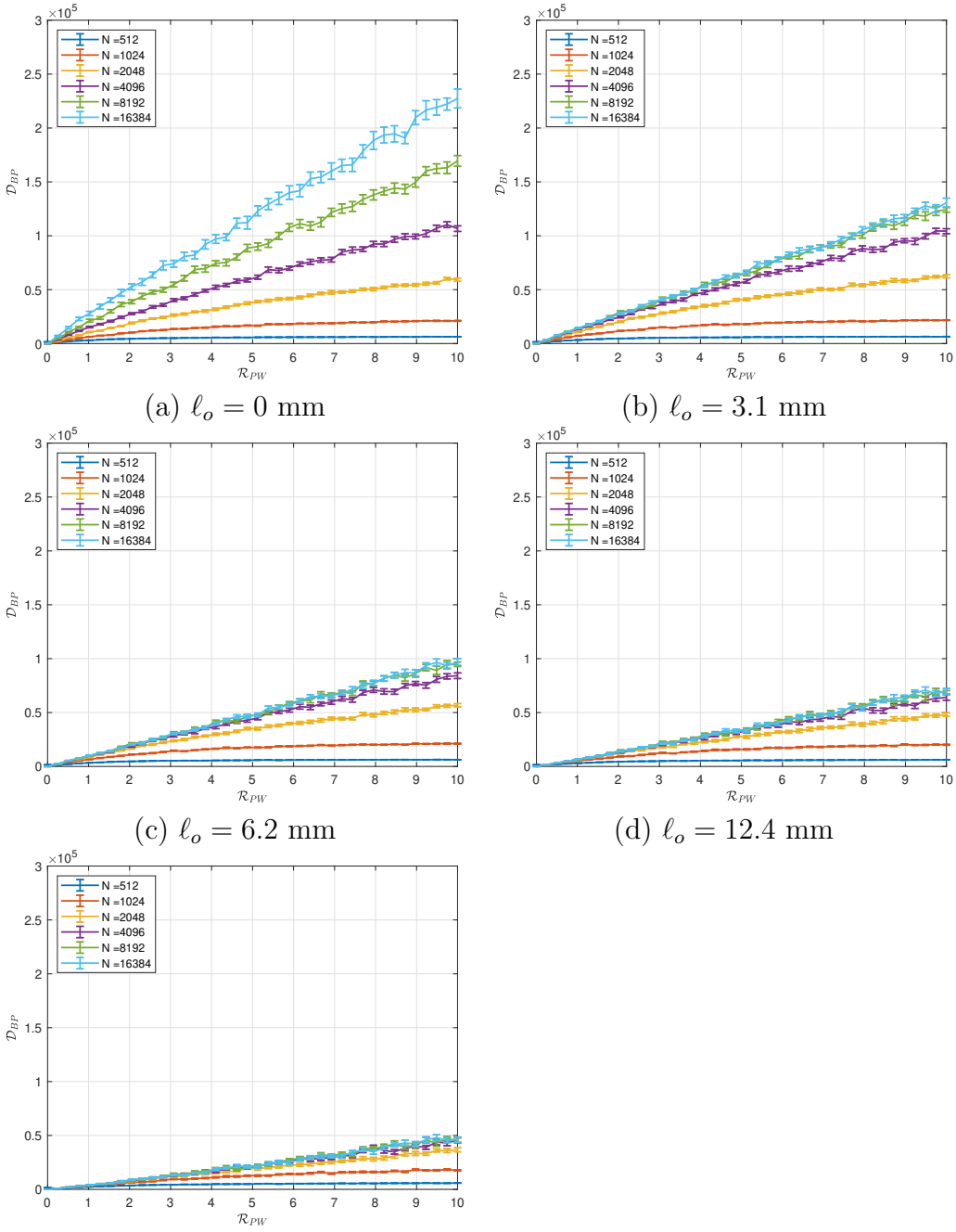

(a) $\ell_o = 0$ mm

(b) $\ell_o = 3.1$ mm

(c) $\ell_o = 6.2$ mm

(d) $\ell_o = 12.4$ mm

(e) $\ell_o = 24.8$ mm

Figure 4.4: Total branch point density, **with spurious branch points removed**, as a function of spherical-wave Rytov number, $\mathcal{R}_{PW}$ for grid resolutions $N = 512$, 1024, 2048, 4096, 8192, and 16,384. In each sub-figure a different inner scale was used such that, **a** Kolmogorov power spectrum with $l_0 = 0$ mm, **(b)** Hill spectrum with $l_0 = 3.1$ mm, **(c)** $l_0 = 6.2$ mm, **(d)** $l_0 = 12.4$ mm, and **(e)** $l_0 = 24.8$ mm.

useful to characterize its behavior. Modelling branch-point density as a function of several other factors, such as aperture size, propagation distance, wavelength and more may allow for a closed-form expression to be developed for branch-point density. Another angle of investigation could be to investigate branch-point density for different source models, like a spherical wave or for a Gaussian beam. A plane wave was used in this work for its simplicity, but a spherical wave or a Gaussian beam would be a more accurate source model in the context of real world beam control applications.

Chapter 5

Conclusions

In Chapter 2 Mellin-transform techniques were used to derive generalized expressions for the total, piston-removed, and piston-and-tilt-removed anisoplanatic error in non-Kolmogorov turbulence with a finite outer scale. These expressions were used to investigate the behavior of the anisoplanatic error when imaging over long horizontal paths where the angular extent of the scene was often many times the isoplanatic angle. By evaluating these expressions it was found that in many cases the anisoplanatic error saturated to a value less than 1 rad^2. This means that, while not actually infinite, the piston-removed and piston-and-tilt-removed isoplanatic angle is often significantly larger than expected. Next it was found that as power-law exponent α increases, the contributions due to piston and tilt dominated the anisoplanatic error expression. Lastly, the size of the outer scale contributed primarily to the piston and

tilt terms. Together, those behaviors imply that when piston and tilt are removed, anisoplanatism was as much as 60% less severe than the classic anisoplanatic error expression predicted for small apertures imaging over long horizontal paths in moderate to strong turbulence.

In Chapter 3, two assumptions made in Chapter 2 were examined. The effects of non-Kolmogorov turbulence and a finite outer scale on angular anisoplanatism in incoherent imaging over long horizontal and slanted-paths was investigated. Generalized expressions for the anisoplanatic error in non-Kolmogorov turbulence were developed from expressions fully derived in Section 2.2 for spherical and plane wave source models. Then the behavior of the anisoplanatic error was compared for upward-looking and downward-looking geometries to a purely horizontal geometry. It was found that using a wavefront with a non-zero radius of curvature increased the effective isoplanatic angle for all cases, regardless of power-law exponent, outer scale size, or turbulence strength. It was also found that anisoplanatism was most severe in the downward-looking case and was least severe in the upward-looking case with the horizontal case in between.

In Chapter 4 wave-optics simulations were used to model the density of branch points as a function of grid resolution and plane-wave Rytov variance in deep turbulence over a long horizontal path. For all cases the branch-density was modelled for five different inner scale values. Overall the results showed that the branch-point density increased

without bound as Rytov variance increased if an ideal, 0 mm inner scale is used. When a non-zero inner scale is used, via a hill spectrum, the growth of the branch point density as a function of increasing plane-wave Rytov variance is significantly reduced. Both of these results counteract the initial hypothesis in[104], that the inclusion of finite inner scale would cause the branch-point density to saturate, because growth without bound seemed unphysical.

This dissertation makes several important contributions to characterizing the behavior of the anisoplanatic error and the branch-point density in deep turbulence. Both of these phenomena can have significant deleterious effects on reconstruction and phase-compensation efforts in incoherent imaging and coherent beam control systems. Because these phenomena are features of deep turbulence, characterizing their behavior is tantamount to better characterizing deep turbulence itself. With a better understanding of deep turbulence, next-generation post-processing and adaptive optics techniques can be developed to counteract turbulence effects in horizontal imaging and beam control scenarios.

5.1 Suggestions for Future Work

The completion of this work does not close the door on any of the problems discussed here and provides several unanswered questions that may be of interest for

future work. Most obviously, it would be valuable to compare the performance of post-processing techniques in scenarios that match the anisoplanatic error saturation regimes observed in Chapters 2 and 3. Simulation could be used to generate images aberrated by deep turbulence over a horizontal path, where traditional theory predicts the isoplanatic angle approaches the diffraction limited sampling rate of the system and therefore recovery techniques should be unsuccessful. Speckle imaging or other post-processing techniques could then be attempted on these images to determine how well these recovery techniques work in cases where the anisoplanatic error saturates and the isoplanatic angle may effectively be infinite.

Other ideas for future work in this area include a larger scale branch point trade space study with the goal of creating a closed-form expression for branch point density. The work here neglects factors like wavelength, aperture size, propagation distance, and source modelling. The first effort to model the branch point density used a propagating Gaussian beam instead of a plane wave, because it is more physically accurate. The Gaussian was unused due to a number of unexplained issues in sampling and beam wander. If these issues could be addressed, along with modelling the effect of wavelength, aperture size, and propagation distance, then it is likely that a closed-form expression or at least a rudimentary scaling law could be developed to predict the density of branch points in a given beam control scenario.

References

[1] J. R. Beck and J. P. Bos, "Angular anisoplanatism in non-kolmogorov turbulence over horizontal paths," *JOSA A*, vol. 37, no. 12, pp. 1937–1949, 2020.

[2] D. L. Fried, "Anisoplanatism in adaptive optics," *JOSA*, vol. 72, no. 1, pp. 52–61, 1982.

[3] R. R. Beland, "Propagation through atmospheric optical turbulence," *Atmospheric Propagation of Radiation*, vol. 2, pp. 157–232, 1993.

[4] G. A. Tyler, "Adaptive optics compensation for propagation through deep turbulence: a study of some interesting approaches," *Optical Engineering*, vol. 52, no. 2, p. 021011, 2012.

[5] G. C. Valley, "Isoplanatic degradation of tilt correction and short-term imaging systems," *Applied Optics*, vol. 19, no. 4, pp. 574–577, 1980.

[6] B. M. Welsh and C. S. Gardner, "Effects of turbulence-induced anisoplanatism

on the imaging performance of adaptive-astronomical telescopes using laser guide stars," *JOSA A*, vol. 8, no. 1, pp. 69–80, 1991.

[7] R. R. Parenti and R. J. Sasiela, "Laser-guide-star systems for astronomical applications," *JOSA A*, vol. 11, no. 1, pp. 288–309, 1994.

[8] D. L. Fried and J. L. Vaughn, "Branch cuts in the phase function," *Applied Optics*, vol. 31, no. 15, pp. 2865–2882, 1992.

[9] J. D. Barchers, D. L. Fried, and D. J. Link, "Evaluation of the performance of hartmann sensors in strong scintillation," *Applied optics*, vol. 41, no. 6, pp. 1012–1021, 2002.

[10] D. L. Fried, "Adaptive optics wave function reconstruction and phase unwrapping when branch points are present," *Optics Communications*, vol. 200, no. 1-6, pp. 43–72, 2001.

[11] W. W. Arrasmith, "Branch-point-tolerant least-squares phase reconstructor," *JOSA A*, vol. 16, no. 7, pp. 1864–1872, 1999.

[12] T. M. Venema and J. D. Schmidt, "Optical phase unwrapping in the presence of branch points," *Optics Express*, vol. 16, no. 10, pp. 6985–6998, 2008.

[13] M. J. Steinbock, M. W. Hyde, and J. D. Schmidt, "Lspv+ 7, a branch-point-tolerant reconstructor for strong turbulence adaptive optics," *Applied optics*, vol. 53, no. 18, pp. 3821–3831, 2014.

[14] M. Spencer, R. Raynor, T. Rhoadarmer, and D. Marker, "Deep-turbulence simulation in a scaled-laboratory environment using five phase-only spatial light modulators," in *Proc. 18th Coherent Laser Radar Conf*, 2016.

[15] V. V. Voitsekhovich, D. Kouznetsov, and D. K. Morozov, "Density of turbulence-induced phase dislocations," *Applied optics*, vol. 37, no. 21, pp. 4525–4535, 1998.

[16] M. F. Spencer, "Wave-optics investigation of turbulence thermal blooming interaction: I. Using steady-state simulations," *Optical Engineering*, vol. 59, no. 8, pp. 1 – 16, 2020.

[17] M. F. Spencer, "Wave-optics investigation of turbulence thermal blooming interaction: Ii. using time-dependent simulations," *Optical Engineering*, vol. 59, no. 8, p. 081805, 2020.

[18] L. C. Andrews and R. L. Phillips, *Laser beam propagation through random media*. SPIE Press Bellingham, WA, 2005.

[19] L. F. Richardson, *Weather prediction by numerical process*. Cambridge university press, 2007.

[20] V. I. Tatarski, *Wave propagation in a turbulent medium*. Courier Dover Publications, 2016.

[21] A. N. Kolmogorov, "The local structure of turbulence in incompressible viscous fluid for very large reynolds numbers," *Cr Acad. Sci. URSS*, vol. 30, pp. 301–305, 1941.

[22] M. C. Roggemann, B. M. Welsh, and B. R. Hunt, *Imaging through turbulence*. CRC press, 1996.

[23] M. S. Belen'kii, S. J. Karis, C. L. Osmon, J. M. Brown II, and R. Q. Fugate, "Experimental evidence of the effects of non-kolmogorov turbulence and anisotropy of turbulence," in *18th Congress of the International Commission for Optics*, vol. 3749, pp. 50–51, International Society for Optics and Photonics, 1999.

[24] F. Dalaudier, C. Sidi, M. Crochet, and J. Vernin, "Direct evidence of "sheets" in the atmospheric temperature field," *Journal of the Atmospheric Sciences*, vol. 51, no. 2, pp. 237–248, 1994.

[25] R. Buser, "Interferometric determination of the distance dependence of the phase structure function for near-ground horizontal propagation at 6328 å," *JOSA*, vol. 61, no. 4, pp. 488–491, 1971.

[26] M. Bester, W. C. Danchi, C. G. Degiacomi, L. J. Greenhill, and C. H. Townes, "Atmospheric fluctuations-empirical structure functions and projected performance of future instruments," *The Astrophysical Journal*, vol. 392, pp. 357–374, 1992.

[27] D. Dayton, B. Pierson, B. Spielbusch, and J. Gonglewski, "Atmospheric structure function measurements with a shack–hartmann wave-front sensor," *Optics letters*, vol. 17, no. 24, pp. 1737–1739, 1992.

[28] W. A. Bernard, B. M. Welsh, M. C. Roggemann, and R. J. Feldmann, "Atmospheric turbulence characterization of a low-altitude long horizontal path," in *Image Propagation through the Atmosphere*, vol. 2828, pp. 198–209, International Society for Optics and Photonics, 1996.

[29] B. E. Stribling, "Laser beam propagation in non-kolmogorov atmospheric turbulence.," tech. rep., AIR FORCE INST OF TECH WRIGHT-PATTERSON AFB OH SCHOOL OF ENGINEERING, 1994.

[30] A. Labeyrie, "Attainment of diffraction limited resolution in large telescopes by fourier analysing speckle patterns in star images," *Astron. Astrophys.*, vol. 6, no. 1, pp. 85–87, 1970.

[31] K. T. Knox and B. J. Thompson, "Recovery of images from atmospherically degraded short-exposure photographs," *The astrophysical journal*, vol. 193, pp. L45–L48, 1974.

[32] G. Weigelt and B. Wirnitzer, "Image reconstruction by the speckle-masking method," *Optics Letters*, vol. 8, no. 7, pp. 389–391, 1983.

[33] G. Ayers, M. Northcott, and J. Dainty, "Knox–thompson and triple-correlation

imaging through atmospheric turbulence," *JOSA A*, vol. 5, no. 7, pp. 963–985, 1988.

[34] G. Ayers and J. C. Dainty, "Iterative blind deconvolution method and its applications," *Optics letters*, vol. 13, no. 7, pp. 547–549, 1988.

[35] T. J. Schulz, "Multiframe blind deconvolution of astronomical images," *JOSA A*, vol. 10, no. 5, pp. 1064–1073, 1993.

[36] T. J. Schulz, B. E. Stribling, and J. J. Miller, "Multiframe blind deconvolution with real data: imagery of the hubble space telescope," *Optics express*, vol. 1, no. 11, pp. 355–362, 1997.

[37] G. Archer, J. P. Bos, and M. C. Roggemann, "Reconstruction of long horizontal-path images under anisoplanatic conditions using multiframe blind deconvolution," *Optical Engineering*, vol. 52, no. 8, p. 083108, 2013.

[38] G. E. Archer, J. P. Bos, and M. C. Roggemann, "Comparison of bispectrum, multiframe blind deconvolution and hybrid bispectrum-multiframe blind deconvolution image reconstruction techniques for anisoplanatic, long horizontal-path imaging," *Optical Engineering*, vol. 53, no. 4, p. 043109, 2014.

[39] R. A. Gonsalves and R. Chidlaw, "Wavefront sensing by phase retrieval," in *Applications of Digital Image Processing III*, vol. 207, pp. 32–39, International Society for Optics and Photonics, 1979.

[40] R. G. Paxman, T. J. Schulz, and J. R. Fienup, "Joint estimation of object and aberrations by using phase diversity," *JOSA A*, vol. 9, no. 7, pp. 1072–1085, 1992.

[41] B. J. Thelen, R. G. Paxman, D. A. Carrara, and J. H. Seldin, "Maximum a posteriori estimation of fixed aberrations, dynamic aberrations, and the object from phase-diverse speckle data," *JOSA A*, vol. 16, no. 5, pp. 1016–1025, 1999.

[42] B. J. Thelen, R. G. Paxman, D. A. Carrara, and J. H. Seldin, "Overcoming turbulence-induced space-variant blur by using phase-diverse speckle," *JOSA A*, vol. 26, no. 1, pp. 206–218, 2009.

[43] J. P. Bos and M. C. Roggemann, "Robustness of speckle-imaging techniques applied to horizontal imaging scenarios," *Optical Engineering*, vol. 51, no. 8, p. 083201, 2012.

[44] R. Stachnik, P. Nisenson, D. Ehn, R. Hudgin, and V. Schirf, "Speckle image reconstruction of solar features," *Nature*, vol. 266, no. 5598, pp. 149–151, 1977.

[45] A. Lambert, F. Li, D. Bowman, and D. Fraser, "Experiments in turbulence induced super-resolution in surveillance imagery," in *28th International Congress on High-Speed Imaging and Photonics*, vol. 7126, p. 712612, International Society for Optics and Photonics, 2009.

[46] J. Stone, P. Hu, S. Mills, and S. Ma, "Anisoplanatic effects in finite-aperture optical systems," *JOSA A*, vol. 11, no. 1, pp. 347–357, 1994.

[47] J. Beck and J. P. Bos, "Saturation of the anisoplanatic error in horizontal imaging scenarios," in *Laser Communication and Propagation through the Atmosphere and Oceans VI*, vol. 10408, p. 104080X, International Society for Optics and Photonics, 2017.

[48] D. L. Fried, "Angular dependence of atmospheric turbulence effect in speckle interferometry," in *International Astronomical Union Colloquium*, vol. 50, pp. 26–1, Cambridge University Press, 1979.

[49] A. Ishimaru, *Wave propagation and scattering in random media*, vol. 2. Academic press New York, 1978.

[50] R. J. Sasiela, "Electromagnetic wave propagation in turbulence: evaluation and application of mellin transforms," in *SPIE Press Monograph Vol. PM171*, SPIE, 2007.

[51] A. Consortini, L. Ronchi, and E. Moroder, "Role of the outer scale of turbulence in atmospheric degradation of optical images," *JOSA*, vol. 63, no. 10, pp. 1246–1248, 1973.

[52] D. M. Winker, "Effect of a finite outer scale on the zernike decomposition of atmospheric optical turbulence," *J. Opt. Soc. Am. A*, vol. 8, pp. 1568–1573, Oct 1991.

[53] J. E. McCrae, C. A. Rice, S. R. Bose-Pillai, and S. T. Fiorino, "Investigating

the outer scale of atmospheric turbulence with a hartmann sensor," in *2019 IEEE Aerospace Conference*, pp. 1–6, IEEE, 2019.

[54] R. J. Sasiela and J. D. Shelton, "Transverse spectral filtering and mellin transform techniques applied to the effect of outer scale on tilt and tilt anisoplanatism," *JOSA A*, vol. 10, no. 4, pp. 646–660, 1993.

[55] M. Abramowitz and I. A. Stegun, *Handbook of mathematical functions: with formulas, graphs, and mathematical tables*, vol. 55. Courier Corporation, 1965.

[56] J. P. Bos and M. C. Roggemann, "Blind image quality metrics for optimal speckle image reconstruction in horizontal imaging scenarios," *Optical Engineering*, vol. 51, no. 10, p. 107003, 2012.

[57] J. R. Beck and J. P. Bos, "Angular anisoplanatism in non-kolmogorov turbulence over horizontal and slant paths," in *Laser Communication and Propagation through the Atmosphere and Oceans IX*, vol. 11506, p. 115060N, International Society for Optics and Photonics, 2020.

[58] I. Toselli, L. C. Andrews, R. L. Phillips, and V. Ferrero, "Free-space optical system performance for laser beam propagation through non-kolmogorov turbulence," *Optical Engineering*, vol. 47, no. 2, p. 026003, 2008.

[59] R. Hufnagel, "Variations of atmospheric turbulence. digest of technical papers," in *Topical meeting on optical propagation through turbulence, university of Colorado, Boulder, CO*, 1974.

[60] D. L. Fried, "Branch point problem in adaptive optics," *JOSA A*, vol. 15, no. 10, pp. 2759–2768, 1998.

[61] J. F. Nye and M. V. Berry, "Dislocations in wave trains," *Proceedings of the Royal Society of London. A. Mathematical and Physical Sciences*, vol. 336, no. 1605, pp. 165–190, 1974.

[62] M. Berry, "Disruption of wavefronts: statistics of dislocations in incoherent gaussian random waves," *Journal of Physics A: Mathematical and General*, vol. 11, no. 1, p. 27, 1978.

[63] N. Baranova, B. Y. Zel'Dovich, A. Mamaev, N. Pilipetskii, and V. Shkukov, "Dislocations of the wavefront of a speckle-inhomogeneous field (theory and experiment)," *Jetp Lett*, vol. 33, no. 4, p. 206, 1981.

[64] N. Baranova and B. Y. Zel'dovich, "Dislocations of the wave-front surface and zeros of the amplitude," *Zh. Eksp. Teor. Fiz.*, vol. 80, pp. 1789–1797, 1981.

[65] N. Baranova, A. Mamaev, N. Pilipetsky, V. Shkunov, and B. Y. Zel'dovich, "Wave-front dislocations: topological limitations for adaptive systems with phase conjugation," *JOSA*, vol. 73, no. 5, pp. 525–528, 1983.

[66] J. F. Nye, J. Hajnal, and J. Hannay, "Phase saddles and dislocations in two-dimensional waves such as the tides," *Proceedings of the Royal Society of London. A. Mathematical and Physical Sciences*, vol. 417, no. 1852, pp. 7–20, 1988.

[67] F. Arecchi, G. Giacomelli, P. Ramazza, and S. Residori, "Vortices and defect statistics in two-dimensional optical chaos," *Physical review letters*, vol. 67, no. 27, p. 3749, 1991.

[68] I. Freund and N. Shvartsman, "Wave-field phase singularities: the sign principle," *Physical Review A*, vol. 50, no. 6, p. 5164, 1994.

[69] N. Shvartsman and I. Freund, "Vortices in random wave fields: nearest neighbor anticorrelations," *Physical review letters*, vol. 72, no. 7, p. 1008, 1994.

[70] I. Freund, "Optical vortices in gaussian random wave fields: statistical probability densities," *JOSA A*, vol. 11, no. 5, pp. 1644–1652, 1994.

[71] I. Freund and N. Shvartsman, "Structural correlations in gaussian random wave fields," *Physical Review E*, vol. 51, no. 4, p. 3770, 1995.

[72] I. Freund, "Saddles, singularities, and extrema in random phase fields," *Physical Review E*, vol. 52, no. 3, p. 2348, 1995.

[73] I. Freund, "Amplitude topological singularities in random electromagnetic wavefields," *Physics Letters A*, vol. 198, no. 2, pp. 139–144, 1995.

[74] N. Heckenberg, M. Vaupel, J. Malos, and C. Weiss, "Optical-vortex pair creation and annihilation and helical astigmatism of a nonplanar ring resonator," *Physical Review A*, vol. 54, no. 3, p. 2369, 1996.

[75] E. Abramochkin and V. Volostnikov, "Spiral-type beams: optical and quantum aspects," *Optics Communications*, vol. 125, no. 4-6, pp. 302–323, 1996.

[76] I. Freund, "Vortex derivatives," *Optics communications*, vol. 137, no. 1-3, pp. 118–126, 1997.

[77] V. Tartakovski and N. Mayer, "Phase dislocations and minimal phase representation of the wave function," *Atmos. Oceanic Opt.*, vol. 8, pp. 231–235, 1995.

[78] V. Tartakovskii and N. Mayer, "Phase dislocations and focal spot," *ATMOSPHERIC AND OCEANIC OPTICS C/C OF OPTIKA ATMOSFERY I OKEANA*, vol. 9, pp. 926–929, 1996.

[79] V. P. Lukin and B. V. Fortes, "The influence of wavefront dislocations on phase conjugation instability with thermal blooming compensation," *Pure and Applied Optics: Journal of the European Optical Society Part A*, vol. 6, no. 1, p. 103, 1997.

[80] B. V. Fortes, "The effects of the wavefront dislocations on the atmospheric adaptive optical systems performance," in *17th Congress of the International Commission for Optics: Optics for Science and New Technology*, vol. 2778, p. 2778DI, International Society for Optics and Photonics, 1996.

[81] M. C. Roggemann and A. C. Koivunen, "Wave-front sensing and deformable-mirror control in strong scintillation," *JOSA A*, vol. 17, no. 5, pp. 911–919, 2000.

[82] Y. Li, "Branch point effect on adaptive correction," in *Advancements in Adaptive Optics*, vol. 5490, pp. 1064–1070, International Society for Optics and Photonics, 2004.

[83] J. D. Barchers, D. L. Fried, and D. J. Link, "Evaluation of the performance of a shearing interferometer in strong scintillation in the absence of additive measurement noise," *Applied optics*, vol. 41, no. 18, pp. 3674–3684, 2002.

[84] E.-O. Le Bigot and W. J. Wild, "Theory of branch-point detection and its implementation," *JOSA A*, vol. 16, no. 7, pp. 1724–1729, 1999.

[85] G. A. Tyler, "Reconstruction and assessment of the least-squares and slope discrepancy components of the phase," *JOSA A*, vol. 17, no. 10, pp. 1828–1839, 2000.

[86] K. Murphy, R. Mackey, and C. Dainty, "Branch point detection and correction using the branch point potential method," in *Atmospheric Propagation V*, vol. 6951, p. 695105, International Society for Optics and Photonics, 2008.

[87] M. Soskin and M. Vasnetsov, "Singular optics," *Progress in optics*, vol. 42, no. 4, pp. 219–276, 2001.

[88] C. Paterson, "Atmospheric turbulence and orbital angular momentum of single photons for optical communication," *Physical review letters*, vol. 94, no. 15, p. 153901, 2005.

[89] N. Simpson, K. Dholakia, L. Allen, and M. Padgett, "Mechanical equivalence of spin and orbital angular momentum of light: an optical spanner," *Optics letters*, vol. 22, no. 1, pp. 52–54, 1997.

[90] G. Gbur and R. K. Tyson, "Vortex beam propagation through atmospheric turbulence and topological charge conservation," *JOSA A*, vol. 25, no. 1, pp. 225–230, 2008.

[91] G. Gbur, "The evolution of vortex beams in atmospheric turbulence," in *Atmospheric Propagation of Electromagnetic Waves II*, vol. 6878, p. 687804, International Society for Optics and Photonics, 2008.

[92] D. W. Oesch, D. J. Sanchez, C. M. Tewksbury-Christle, and P. R. Kelly, "The aggregate behavior of branch points: branch point density as a characteristic of an atmospheric turbulence simulator," in *Advanced Wavefront Control: Methods, Devices, and Applications VII*, vol. 7466, p. 746606, International Society for Optics and Photonics, 2009.

[93] D. J. Sanchez and D. W. Oesch, "The aggregate behavior of branch points: the creation and evolution of branch points," in *Advanced Wavefront Control: Methods, Devices, and Applications VII*, vol. 7466, p. 746605, International Society for Optics and Photonics, 2009.

[94] D. W. Oesch, D. J. Sanchez, and C. M. Tewksbury-Christle, "Aggregate behavior of branch points-persistent pairs," *Optics express*, vol. 20, no. 2, pp. 1046–1059, 2012.

[95] D. W. Oesch, D. J. Sanchez, and C. L. Matson, "The aggregate behavior of branch points-measuring the number and velocity of atmospheric turbulence layers," *Optics express*, vol. 18, no. 21, pp. 22377–22392, 2010.

[96] D. W. Oesch, D. J. Sanchez, C. M. Tewksbury-Christle, and P. R. Kelly, "The aggregate behavior of branch points: altitude and strength of atmospheric turbulence layers," in *Advanced Wavefront Control: Methods, Devices, and Applications VIII*, vol. 7816, p. 781605, International Society for Optics and Photonics, 2010.

[97] D. W. Oesch, C. M. Tewksbury-Christle, D. J. Sanchez, and P. R. Kelly, "Aggregate behavior of branch points: characterization in wave optical simulation," *Optical Engineering*, vol. 51, no. 10, p. 106001, 2012.

[98] D. W. Oesch and D. J. Sanchez, "Creating well-defined orbital angular momentum states with a random turbulent medium," *Optics express*, vol. 20, no. 11, pp. 12292–12302, 2012.

[99] D. W. Oesch, D. J. Sanchez, A. L. Gallegos, J. M. Holzman, T. J. Brennan, J. C. Smith, W. J. Gibson, T. C. Farrell, and P. R. Kelly, "Creation of photonic

orbital angular momentum by distributed volume turbulence," *Optics express*, vol. 21, no. 5, pp. 5440–5455, 2013.

[100] A. Majumdar and S. J. Kirkpatrick, "Optical vortices as potential indicators of biophysical dynamics," in *Dynamics and Fluctuations in Biomedical Photonics XIV*, vol. 10063, p. 1006306, International Society for Optics and Photonics, 2017.

[101] A. Majumdar and S. J. Kirkpatrick, "Statistical studies on optical vortices in dynamic speckle fields," *Journal of Biomedical Photonics & Engineering*, vol. 4, no. 2, 2018.

[102] A. Majumdar, *Optical Vortex and Poincaré Analysis for Biophysical Dynamics*. PhD thesis, Michigan Technological University, Houghton MI, 2019.

[103] J. D. Schmidt, *Numerical simulation of optical wave propagation with examples in MATLAB*. SPIE Press Bellingham, Washington, USA, 2010.

[104] J. R. Beck, M. F. Spencer, J. P. Bos, and T. Brennan, "Investigation of branch-point density using traditional wave-optics techniques," in *Unconventional and Indirect Imaging, Image Reconstruction, and Wavefront Sensing 2018*, vol. 10772, p. 1077206, International Society for Optics and Photonics, 2018.

[105] J. P. Bos, M. C. Roggemann, and V. R. Gudimetla, "Anisotropic non-kolmogorov turbulence phase screens with variable orientation," *Applied optics*, vol. 54, no. 8, pp. 2039–2045, 2015.

Appendix A

Mellin Transform Expressions for Plane Wave Angular Anisoplanatic Error

A.1 Some Useful Mellin Transform Expressions

Below are some Mellin Transforms and useful properties used throughout this work relating to Bessel function of the first kind $J_v(x)$ and modified Bessel functions of the

second kind $K_v(x)$,

$$J_v(x) \to 2^{s-1}\Gamma\begin{bmatrix} s/2+v/2 \\ v/2+1-s/2 \end{bmatrix}, -Re\{v\} < Re\{s\} < 3/2 \tag{A.1.1}$$

$$J_v^2(x) \to \frac{1}{2\sqrt{\pi}}\Gamma\begin{bmatrix} s/2+v, 1/2-s/2 \\ v+1-s/2, 1-s/2 \end{bmatrix}, -2Re\{v\} < Re\{s\} < 1 \tag{A.1.2}$$

$$(1+x)^{-p} \to \frac{\Gamma[s, p-s]}{\Gamma[p]}, 0 < Re\{s\} < Re\{p\} \tag{A.1.3}$$

$$\begin{aligned} K_v(x) &= \frac{1}{4}\frac{1}{2\pi j}\int_C \mathrm{d}s\Gamma[s/2+v/2, s/2-v/2](x/2)^{-s} \\ &\times \frac{1}{2}\sum_{n=0}^{\infty}\frac{(-1)^n}{n!}\left(\left(\frac{x}{2}\right)^{2n+v}\Gamma[-n-v] + \left(\frac{x}{2}\right)^{2n-v}\Gamma[-n+v]\right) \end{aligned} \tag{A.1.4}$$

A.2 Relating the Index of Refraction Spectrum and the Phase Spectrum

The phase PSD, $\Phi_\phi(\kappa)$, can be expressed in terms of its refractive index spectrum, $\Phi_n(\kappa)$, transverse dimension, L, and wavenumber k_0, as

$$\Phi_\phi(\kappa) = 2\pi^2 k^2 L\Phi_n(\kappa). \tag{A.2.1}$$

In both Eqs. (A.2.1) and (2.4) κ is the PSD spatial frequency and has units of radians per meter. We wish to describe the refractive index spectrum, $\Phi_n(\kappa)$, in Eq. (2.11) in terms of a characteristic length, $\hat{r}_0$. From Bos[105] we can write the generalized model for the phase PSD, under the assumption of constant turbulence along the path, in a non-Kolmogorov power law medium as

$$\Phi_\phi(\kappa,\alpha) = B(\alpha)c_1(\alpha)\hat{r}_0^{2-\alpha}\left(\kappa^2+\kappa_0^2\right)^{-\alpha/2} \tag{A.2.2}$$

where

$$B(\alpha) = \frac{\Gamma\left[\frac{\alpha}{2}\right]}{2^{2-\alpha}\pi\alpha\Gamma\left[-\frac{\alpha}{2}\right]} \tag{A.2.3}$$

is a parameter that maintains consistency between the structure function and PSD descriptions and

$$c_1(\alpha) = 2\left(\frac{8}{\alpha-2}\Gamma\left[\frac{2}{\alpha-2}\right]\right)^{\frac{\alpha-2}{2}}, \tag{A.2.4}$$

is a constant equal to the value of the plane wave, wave structure function (WSF) at a separation equal to the characteristic length, $\hat{r}_0$. $c_1(\alpha)$ was previously obtained by Stribling [29]. Substituting Eq. (A.2.2) into Eq. (A.2.1) and solving for $\Phi_n(\kappa,\alpha)$ provides

$$\Phi_n(\kappa,\alpha) = \frac{B(\alpha)c_1(\alpha)\hat{r}_0^{2-\alpha}\left(\kappa^2+\kappa_0^2\right)^{-\alpha/2}}{2\pi^2k_0^2L}. \tag{A.2.5}$$

Equation (A.2.5) can now be used to rewrite Eq. (2.11) as Eq. (2.12).

A.3 Analytic Expression for Plane Wave Phase Variance with a Finite Outer Scale

An analytic solution to Eq. (2.12) is readily available using Mellin transforms. We begin by expanding the term in the second integral to arrive at the intermediate result:

$$I_A(\alpha) = \int \kappa \left(\kappa^2 + \kappa_0^2\right)^{-\alpha/2} \mathrm{d}\kappa - \int \kappa \left(\kappa^2 + \kappa_0^2\right)^{-\alpha/2} \mathrm{J}_0(\kappa\theta z)\, \mathrm{d}\kappa \tag{A.3.1}$$

The solution to the first integral is trivial to evaluate with integral tables and can be found to be

$$I_1(\alpha) = \frac{\kappa_0^{2-\alpha}}{-2+\alpha}. \tag{A.3.2}$$

The solution to the second integral is accomplished by exploiting the convolution property of Mellin transforms. We begin by substituting $\omega = \kappa\theta z$ into the second equation to get

$$I_2(\alpha) = \frac{\kappa_0^{-\alpha}}{(\theta z)^2} \int_0^\infty \frac{\mathrm{d}\omega}{\omega} \omega^{-\alpha} \mathrm{J}_0(\omega) \left[1 + \left(\frac{\kappa\theta z}{\omega}\right)^{-2}\right]^{-\alpha/2}. \tag{A.3.3}$$

The expression is now in the general form of a Mellin convolution integral. The Mellin transforms of each function can be found from Eqs. (A.1.1) and (A.1.3) and these

can be used to recast Eq. (A.3.3) into an integral in the complex plane as

$$\begin{aligned} I_2(\alpha) =& \frac{-\kappa_0^{-\alpha}}{2(\theta z)^2 \Gamma\left[\frac{\alpha}{2}\right]} \frac{1}{2\pi j} \int_C \mathrm{d}s \left(\frac{\kappa_0 \theta L}{2}\right)^{-s} \\ & \times \Gamma\left[\frac{s}{2}+1, \frac{\alpha}{2}+\frac{s}{2}\right], \end{aligned} \tag{A.3.4}$$

To perform the pole residue integration, we must determine which direction to close the path of integration. This is accomplished by finding the sum of coefficients of s in the denominator and subtracting that from the sum of coefficients of s in the numerator. In this case $\Delta = 1$, which means the integration path can be closed to the left and the pole residues can be found for the poles $s = -2n - 2$ and $s = -2n - \alpha$. This can be simplified if we recognize that the integral is actually just the inverse Mellin transform, given in Eq. (A.1.4), of $\mathrm{K}_{1-\frac{\alpha}{2}}(\kappa_0 \theta z)$ when $s \to s - \frac{\alpha}{2} + 2$, which gives

$$I_2(\alpha) = \frac{2^{1-\frac{\alpha}{2}} \left(\frac{\kappa_0}{\theta z}\right)^{1-\frac{\alpha}{2}} \mathrm{K}_{1-\frac{\alpha}{2}}[\theta z \kappa_0]}{\Gamma\left[\frac{\alpha}{2}\right]}. \tag{A.3.5}$$

Lastly, Eq. (A.3.2) and Eq. (A.3.5) can be substituted into Eq. (A.3.1) to provide an expression for $I_A(\alpha)$ as

$$I_A(\alpha) = \frac{\kappa_0^{2-\alpha}}{-2+\alpha} - \frac{2^{1-\frac{\alpha}{2}} \left(\frac{\kappa_0}{\theta z}\right)^{1-\frac{\alpha}{2}} \mathrm{K}_{1-\frac{\alpha}{2}}[\theta z \kappa_0]}{\Gamma\left[\frac{\alpha}{2}\right]} \tag{A.3.6}$$

Using Eq. (A.3.6), we can now rewrite Eq. (2.12) as Eq. (2.13).

A.4 Analytic Expression for Plane Wave Piston Phase Variance with a Finite Outer Scale

An analytic solution to Eq. (2.15) is available using the properties of the Mellin convolution theorem and the process outlined in [50]. We begin by restating the integral of interest

$$I_P = \int_0^\infty \mathrm{d}\kappa\kappa \left(\kappa^2 + \kappa_0^2\right)^{-\alpha/2} \left(1 - \mathrm{J}_0\left(\kappa\theta z\right)\right) \left[\frac{2\mathrm{J}_1\left(\kappa D/2\right)}{\kappa D/2}\right]^2 . \tag{A.4.1}$$

By making the variable substitutions $d = \theta L$, $\omega = \kappa d$, $2\pi d/L_0$, and $x = 2d/D$ Eq. (A.4.1) can be recast in terms of three variables,

$$I_P = \frac{-16 d^\alpha}{D^2} \int_0^\infty \frac{\mathrm{d}\omega}{\omega} \omega^{-\alpha} \left(\mathrm{J}_0\left(\omega\right) - 1\right) \mathrm{J}_1^2\left(\omega/x\right) \left[1 + \left(\frac{y}{\omega}\right)^2\right]^{\frac{-\alpha}{2}} . \tag{A.4.2}$$

From inspection we can see that Eq. (A.4.2) is in now in the general form of a Mellin convolution integral of three functions in two planes. We identify each of the three functions and their Mellin transforms , denoted by $M[h(x)] \rightarrow H\left(s\right)$, below. From [50] we substitute s with $s + t$ for the first function's transform and s with t for the third function's transform.

$$h_0(\omega) = \omega^{-\alpha} \left(\mathrm{J}_0(\omega) - 1\right) \tag{A.4.3}$$

$$H_0\left(s+t\right)=\frac{2^s2^t}{2^{1+\alpha}}\frac{\Gamma\left[s/2+t/2-\alpha/2*\right]}{\Gamma\left[-s/2-t/2+\alpha/2+1\right]} \tag{A.4.4}$$

$$h_1(\omega)=\left[1+\left(\frac{y}{\omega}\right)^2\right]^{\alpha/2} \tag{A.4.5}$$

$$H_1(s)=\frac{y^{-s}}{2}\frac{\Gamma\left[s\right]\Gamma\left[\alpha/2-s\right]}{\Gamma[\alpha/2]} \tag{A.4.6}$$

$$h_2(\omega)=\mathrm{J}_1^2(\omega/x) \tag{A.4.7}$$

$$H_2(t)=\frac{x^-t}{2\sqrt{\pi}}\frac{\Gamma[-t+1]\Gamma[1/2+t]}{\Gamma[2+t]\Gamma[1+t]} \tag{A.4.8}$$

Using these transforms and substituting $s \rightarrow 2s$ and $t \rightarrow 2t$, Eq. (A.4.2) can be converted into an integral in two complex planes as

$$\begin{aligned} I_P = I_{P_A}\frac{1}{(2\pi j)^2}\int_{C_1}\int_{C_2}\mathrm{d}s\mathrm{d}t\left(\frac{\pi d}{L_0}\right)^{-2s}\left(\frac{d}{D}\right)^{-2t} \\ \times\Gamma\left[\begin{array}{c} s+t-\frac{\alpha}{2}*,-t+1,\frac{1}{2}+t,s,\frac{\alpha}{2}-s \\ \\ 2+t,1+t,-s-t+\frac{\alpha}{2}+1 \end{array}\right], \end{aligned} \tag{A.4.9}$$

where

$$I_{P_A}=\frac{-16d^\alpha(2)(2)}{D^2 2^{1+\alpha}(2)(2)\Gamma[\alpha/2]}=\frac{-2^{3-\alpha}d^\alpha}{D^2\Gamma[\alpha/2]}, \tag{A.4.10}$$

and the Γ function is a ratio of the product of γ functions at each of the comma separated values. The asterisk denotes that the path of integration passes between the first and second pole of the Gamma function at that value. Next, the are eight

possible two poles are:

$$
\begin{aligned}
&(1) - s + \frac{\alpha}{2} = -m; t + \frac{1}{2} \\
&(2) - s + \frac{\alpha}{2} = -m; -t + 1 = -n \\
&(3) - s + \frac{\alpha}{2} = -m; s + t - \frac{\alpha}{2} = -n* \\
&(4) s = -m; \frac{1}{2} + t = -n \\
&(5) s = -m; -t + 1 = -n \\
&(6) s = -m; s + t - \frac{\alpha}{2} = -n* \\
&(7) t + \frac{1}{2} = -n; s + t - \frac{\alpha}{2} = -m* \\
&(8) - t + 1 = -n; s + t - \frac{\alpha}{2} = -m * .
\end{aligned}
\tag{A.4.11}
$$

The m and n terms are integers that vary from 0 to ∞, while the asterisk after a term means that the index varies from 1 to ∞ on one side of the path of integration,

and is 0 on the other. We list the general terms of the possible series as:

$$
\begin{aligned}
&(1)\left(\frac{d}{D}\right)^{2n}\left(\frac{L_0}{\pi d}\right)^{2m} F(0,2),\\
&(2)\left(\frac{D}{d}\right)^{2n}\left(\frac{L_0}{\pi d}\right)^{2m} F(0,2),\\
&(3)\left(\frac{d}{D}\right)^{2n*}\left(\frac{L_0}{\pi d}\right)^{2m} F(0,2),\\
&(4)\left(\frac{d}{D}\right)^{2n}\left(\frac{\pi d}{L_0}\right)^{2m} F(0,-2),\\
&(5)\left(\frac{D}{d}\right)^{2n}\left(\frac{\pi d}{L_0}\right)^{2m} F(0,-2),\\
&(6)\left(\frac{d}{D}\right)^{2n*}\left(\frac{\pi D}{L_0}\right)^{2m} F(0,-2),\\
&(7)\left(\frac{L_0}{\pi D}\right)^{2n}\left(\frac{\pi d}{L_0}\right)^{2m*} F(2,-2), and\\
&(8)\left(\frac{\pi D}{L_0}\right)^{2n}\left(\frac{\pi d}{L_0}\right)^{2m*} F(-2,-2).
\end{aligned}
\tag{A.4.12}
$$

Here the $F(\Omega_n, \Omega_m) = (n!)^{\Omega_n}(m!)^{\Omega_m}$ function denotes the factorial behavior of series terms of the summation indices. This above list produces the parameters relevant to the problem. The new parameter above is $\pi D/L_0$. To determine which pole residues should be applied, we apply the convergence range rule given by Sasiela [50] to produce Table A.1. From the numeric evaluation in Sections 2.3 we recognize we are only interested in the case where $d/D < 1$, where $\theta < 100\mu$rads when $L = 1000$m. This allows us to ignore asymptotic series 2 and Taylor series 5. From here we divide our evaluation into two regimes. In the first regime $\pi d/L_0 > 1$, and asymptotic series

Table A.1
Series ranges of applicability for most rapid convergence for piston phase variance with outer scale present.

2-Pole Set	Solution Type	Parameter	Range
1	Asymp	$\pi d/L_0 > 1$	$d < D$
2	Asymp	$\pi d/L_0 > 1$	$d > D$
3	Asymp	$\pi D/L_0 > 1$	$d < D$
4	Taylor	$\pi d/L_0 < 1$	$d < D$
5	Taylor	$\pi d/L_0 < 1$	$d > D$
6	Taylor	$\pi D/L_0 < 1$	$d < D$
7	Asymp	$\pi D/L_0 > 1$	$\pi d/L_0 < 1$
8	Taylor	$\pi D/L_0 < 1$	$\pi d/L_0 < 1$

1 and 3 and a steepest descent contribution apply. In the second regime $\pi d/L_0 < 1$ and Taylor 4, 6, 7 and asymptotic series 8 plus a steepest descent contribution apply. The series that result from the evaluation of the residues at 2-poles 1, 3, 4, 6, 7, and 8 are given as:

$$I_{P,1} = I_{P_A} S(0,0a) \left(\frac{d}{D}\right)^{2n+1} \left(\frac{L_0}{\pi d}\right)^{2m+\alpha} \times \Gamma \left[\begin{array}{c} \frac{1}{2}+m-n, \frac{3}{2}+n, \frac{\alpha}{2}+m \\ \\ \frac{3}{2}-n, \frac{1}{2}-n, \frac{3}{2}-m+n \end{array} \right]$$

$$I_{P,3} = I_{P_A} \left(\frac{L_0}{\pi d}\right)^{\alpha} S(1,0a) \left(\frac{d}{D}\right)^{2n} \left(\frac{L_0}{\pi D}\right)^{2m} \times \Gamma \left[\begin{array}{c} n+m+1, \frac{1}{2}-n-m, \frac{\alpha}{2}+m \\ \\ 2-n-m, 1-n-m, 1+n \end{array} \right]$$

$$I_{P,4} = I_{P_A} S(0,0) \left(\frac{d}{D}\right)^{2n+1} \left(\frac{\pi d}{L_0}\right)^{3m} \times \Gamma \left[\begin{array}{c} -m-n-\frac{1}{2}-\frac{\alpha}{2}, n+\frac{3}{2}, \frac{\alpha}{2}+m \\ -n+\frac{3}{2}, -n+\frac{1}{2}, m+n+\frac{\alpha}{2}+\frac{3}{2} \end{array} \right]$$

$$I_{P,6} = I_{P_A} S(1,0) \left(\frac{d}{D}\right)^{2n-\alpha} \left(\frac{\pi D}{L_0}\right)^{2m} \times \Gamma \left[\begin{array}{c} n-\frac{\alpha}{2}-m+1, -n+m+\frac{\alpha}{2}+\frac{1}{2}, \frac{\alpha}{2}+m \\ 2-n+\frac{\alpha}{2}+m, 1-n+\frac{\alpha}{2}+m, 1+n \end{array} \right]$$

$$I_{P,7} = I_{P_A} \left(\frac{d}{D}\right) S(0a,1) \left(\frac{L_0}{\pi D}\right)^{2n} \left(\frac{\pi d}{L_0}\right)^{2m-\alpha-1} \times \Gamma \left[\begin{array}{c} n+\frac{3}{2}, -m+\frac{\alpha}{2}+n+\frac{1}{2}, m-n-\frac{1}{2} \\ -n+\frac{3}{2}, -n+\frac{1}{2}, 1+m \end{array} \right]$$

$$I_{P,8} = I_{P_A} S(0,1) \left(\frac{\pi D}{L_0}\right)^{2n+4} \left(\frac{\pi d}{L_0}\right)^{2m-\alpha} \times \Gamma \left[\begin{array}{c} n+\frac{3}{2}, -m+\frac{\alpha}{2}-1-n, m+1+n \\ 3+n, 2+n, 1+m \end{array} \right].$$

In the above series,

$$S\left(p_1, p_2\right) = \sum_{n=p_1}^{\infty} \sum_{m=p_2}^{\infty} \frac{(-1)^{n+m}}{n!m!},$$

and the a value placed next to the limit indicates that the series is asymptotic so only a finite number of terms should be summed for that series. From inspection of the series, we also recognize that in the $\pi d/L_0 > 1$ regime the seventh and eighth

two-poles provide series of type C_3. These terms are given by

$$C_{3,7} = I_{P_A}\left(\frac{d}{D}\right)\left(\frac{L_0}{\pi d}\right)^{\alpha+1} S(0a)\left(\frac{L_0}{\pi D}\right)^{2n}\Gamma\left[\begin{array}{c} n+\frac{3}{2}, \frac{\alpha}{2}+n+\frac{1}{2}, -n-\frac{1}{2} \\ -n+\frac{3}{2}, -n+\frac{1}{2}, 1 \end{array}\right], \tag{A.4.13}$$

and

$$C_{3,8} = I_{P_A}\left(\frac{L_0}{\pi d}\right)^{\alpha} S(0)\left(\frac{\pi D}{L_0}\right)^{2n+4}\Gamma\left[\begin{array}{c} n+\frac{3}{2}, \frac{\alpha}{2}-1-n, 1+n \\ 3+n, 2+n, 1 \end{array}\right]. \tag{A.4.14}$$

The series of type C_3 simply means that because the summation in m in a particular two-pole starts at 1 when $\pi d/L_0 < 1$, then an identical series where $m = 0$ must be included when $\pi d/L_0 > 1$.

Next we find the steepest descent contributions in each regime. For the first regime where $\pi d/L_0 > 1$ we find that the ratio of s-poles, Δ_s and Δ_t are both negative, which makes evaluating Eq. (A.4.1) for a steepest descent contribution difficult. From [50] we know that this can be remedied by substituting $s \to -s$ and $t \to -t$ in Eq. (A.4.9), which leads to

$$\begin{aligned} I_{P_{SD}} = I_{P_A}\frac{1}{(2\pi j)^2}\int_{C_1}\int_{C_2} \mathrm{d}s\mathrm{d}t \left(\frac{\pi d}{L_0}\right)^{2s}\left(\frac{d}{D}\right)^{2t} \\ \times\Gamma\left[\begin{array}{c} -s-t-\frac{\alpha}{2}*, t+1, \frac{1}{2}-t, -s, \frac{\alpha}{2}+s \\ 2-t, 1-t, s+t+\frac{\alpha}{2}+1 \end{array}\right], \end{aligned} \tag{A.4.15}$$

where $\Delta_s = 0$ and $\Delta_t = 1$ now and the integral can be evaluated sequentially. Accordingly, Eq. (A.4.15) is rewritten as

$$I_{P_{SD1}} = I_{P_A} \frac{1}{2\pi j} \int_{C_2} \mathrm{d}s \Gamma \left[-s, \frac{\alpha}{2} + s \right] \left(\frac{L_0}{\pi d} \right)^{-2s} I_{P_{SD2}}, \tag{A.4.16}$$

where

$$I_{P_{SD2}} = \frac{1}{2\pi j} \int_{C_1} \mathrm{d}t \Gamma \left[\begin{array}{c} -s - t - \frac{\alpha}{2}*, t + 1, \frac{1}{2} - t \\ 2 - t, 1 - t, s + t + \frac{\alpha}{2} + 1 \end{array} \right] \left(\frac{D}{d} \right)^{-2t}. \tag{A.4.17}$$

Using the steepest descent equation from Sasiela[50, p. 141,Eq. 5.94,] Eq. (A.4.17) is found to be

$$I_{P_{SD2}} \approx \frac{-1}{\sqrt{\pi}} \left(\frac{d}{D} \right)^{\frac{-1}{2}} \sin \left[2 \left(\frac{d}{D} \right)^{\frac{1}{2}} \right] \tag{A.4.18}$$

Here, $I_{P_{SD2}}$ does not depend upon s and the evaluation of Eq. (A.4.16) becomes trivial. Because $\Delta_s = 0$ and $L_0/\pi d < 1$, the contour is closed to the left and the pole residues are evaluated at the point $s = -m - \frac{\alpha}{2}$, which gives

$$\begin{aligned} I_{P_{SD}}(L_0/\pi d < 1) \approx & \frac{-I_{P_A}}{\sqrt{\pi}} \sin \left[2 \left(\frac{d}{D} \right)^{\frac{1}{2}} \right] \left(\frac{d}{D} \right)^{\frac{-1}{2}} \left(\frac{L_0}{\pi d} \right)^{\alpha} \\ & \times S(0) \Gamma \left[m + \frac{\alpha}{2} \right] \left(\frac{L_0}{\pi d} \right)^{2m}, \end{aligned} \tag{A.4.19}$$

For the other regime where $L_0/\pi d > 1$ the procedure from Eq. (A.4.15) to (A.4.19) is identical, except the contour is closed to the right and the pole residues are evaluated

at the point $s = m$ to give

$$I_{P_{SD}}(L_0/\pi d > 1) \approx \frac{-I_{P_A}}{\sqrt{\pi}} \sin\left[2\left(\frac{d}{D}\right)^{\frac{-1}{2}}\right]\left(\frac{d}{D}\right)^{\frac{1}{4}}\left(\frac{L_0}{\pi d}\right)^{\alpha} \times S(0)\Gamma\left[m+\frac{\alpha}{2}\right]\left(\frac{L_0}{\pi d}\right)^{2m}. \tag{A.4.20}$$

All of the above can be put together with Eq. (2.15)to acquire the final expressions for plane wave piston phase variance with outer scale as follows,

$$\sigma^2_{\phi,P}(\theta,\alpha) = 4B(\alpha)c_1(\alpha)\int_0^L \mathrm{d}z \frac{\hat{r}_0^{2-\alpha}}{L} \times I_P \tag{A.4.21}$$

where

$$I_P = -\begin{cases} I_{P,1} + I_{P,3} + I_{P_{SD}}[L_0/\pi d < 1] + C_{3,7} + C_{3,8} & \frac{\pi d}{L_0} > 1 \\ I_{P,4} + I_{P,6} + I_{P,7} + I_{P,8} + I_{P_{SD}}[L_0/\pi d > 1] & \frac{\pi d}{L_0} < 1. \end{cases} \tag{A.4.22}$$

There are several things to note about this equation. First, the sets of summations in each of the I_P equations must be carried out for each equation until desired accuracy is achieved. This can result in very long equations, even when only a few terms of each series are wanted, but can remain relatively compact when evaluated via software like Mathematica. In this case, five terms of each series provided accuracy within 1% of the results achieved through numerical integration. Second, while the equations corresponding to Taylor series can be evaluated for as many terms as desired, the asymptotic series should only be evaluated for several terms. As the number of terms

increase, the error in the value of the integral decreases and then at some point it begins to increase. This point, n_o is defined from the location of the steepest-descent path for a given parameter value. In practice, a few terms of the asymptotic series are sufficient to give accurate results. Lastly, the negative factor applied to I_P is to account for flipping the order of 1 and $\mathrm{J}_0(\kappa\theta L)$ in Eq. (A.4.2).

A.5 Analytic Expression for Plane Wave Tilt Phase Variance with a Finite Outer Scale

Much like Appendix A.4 an analytic solution for Eq. (2.17) is readily available using the Mellin convolution theorem. We begin here by restating the original integral for plan wave tilt phase variance as

$$I_T = \int_0^\infty \mathrm{d}\kappa \left(\kappa^2 + \kappa_0^2\right)^{-\alpha/2} \left(1 - J_0\left(\kappa\theta L\right)\right) \left[\frac{4J_2\left(\kappa D/2\right)}{\kappa D/2}\right]^2. \tag{A.5.1}$$

By making the variable substitutions $d = \theta L$, $\omega = \kappa d$, $2\pi d/L_0$, and $x = 2d/D$ Eq. (A.4.1) can be recast in terms of three variables,

$$I_T = \frac{-64d^\alpha}{D^2} \int_0^\infty \frac{\mathrm{d}\omega}{\omega} \omega^{-\alpha} \left(\mathrm{J}_0\left(\omega\right) - 1\right) \mathrm{J}_2^2\left(\omega/x\right) \left[1 + \left(\frac{y}{\omega}\right)^2\right]^{\frac{-\alpha}{2}}. \tag{A.5.2}$$

We immediately recognize that the only difference between Eq. (A.5.2) and Eq. (A.4.2) is that of a second order Bessel function versus a first order Bessel function, both of the first kind. Looking at Eq. (A.1.2), it is apparent that there is no difference in the number or sign of the poles and zeroes when using a $J_2(x)$ versus a $J_1(x)$ function. When fully evaluated, both the integral for tilt and the one for piston require series that are nearly identical in identical regions. For brevity we show only the series that result from the evaluation of the residues at relevant two-poles, the steepest descent contributions, the series of type C_3 that contribute, and the final expression for the integral. Equation (A.5.2) after substituting $s \to 2s$ and $t \to 2t$ is

$$I_T = I_{T_A} \frac{1}{(2\pi j)^2} \int_{C_1} \int_{C_2} \mathrm{d}s\mathrm{d}t \left(\frac{\pi d}{L_0}\right)^{-2s} \left(\frac{d}{D}\right)^{-2t} \times \Gamma \left[\begin{array}{c} s+t-\frac{\alpha}{2}*, -t+2, \frac{1}{2}+t, s, \frac{\alpha}{2}-s \\ 3+t, 1+t, -s-t+\frac{\alpha}{2}+1 \end{array} \right]. \tag{A.5.3}$$

where

$$I_{T_A} = \frac{-64 d^{\alpha}(2)(2)}{D^2 2^{1+\alpha}(2)(2)\Gamma[\alpha/2]} = \frac{-2^{5-\alpha} d^{\alpha}}{D^2 \Gamma[\alpha/2]}, \tag{A.5.4}$$

The series that result from evaluation of the residues at relevant two poles are

$$I_{T,1} = I_{T_A} S(0,0a) \left(\frac{d}{D}\right)^{2n+1} \left(\frac{L_0}{\pi d}\right)^{2m+\alpha} \Gamma \left[\begin{array}{c} \frac{-1}{2}+m-n, \frac{-5}{2}+n, \frac{\alpha}{2}+m \\ \frac{5}{2}-n, \frac{1}{2}-n, \frac{3}{2}-m+n \end{array} \right]$$

$$I_{T,3} = I_{T_A} \left(\frac{L_0}{\pi d}\right)^{\alpha} S(1,0a) \left(\frac{d}{D}\right)^{2n} \left(\frac{L_0}{\pi D}\right)^{2m} \Gamma \left[\begin{array}{c} n+m+2, \frac{1}{2}-n-m, \frac{\alpha}{2}+m \\ 3-n-m, 1-n-m, 1+n \end{array} \right]$$

$$I_{T,4} = I_{T_A} S(0,0) \left(\frac{d}{D}\right)^{2n+1} \left(\frac{\pi d}{L_0}\right)^{3m} \Gamma \left[\begin{array}{c} -m-n-\frac{1}{2}-\frac{\alpha}{2}, n+\frac{5}{2}, \frac{\alpha}{2}+m \\ -n+\frac{5}{2}, -n+\frac{1}{2}, m+n+\frac{\alpha}{2}+\frac{3}{2} \end{array} \right]$$

$$\begin{aligned} I_{T,6} =& I_{T_A} S(1,0) \left(\frac{d}{D}\right)^{2n-\alpha} \left(\frac{\pi D}{L_0}\right)^{2m} \\ & \times \Gamma \left[\begin{array}{c} n-\frac{\alpha}{2}-m+2, -n+m+\frac{\alpha}{2}+\frac{1}{2}, \frac{\alpha}{2}+m \\ 3-n+\frac{\alpha}{2}+m, 1-n+\frac{\alpha}{2}+m, 1+n \end{array} \right] \end{aligned}$$

$$\begin{aligned} I_{T,7} =& I_{T_A} \left(\frac{d}{D}\right) S(0a,1) \left(\frac{L_0}{\pi D}\right)^{2n} \left(\frac{\pi d}{L_0}\right)^{2m-\alpha-1} \\ & \times \Gamma \left[\begin{array}{c} n+\frac{5}{2}, -m+\frac{\alpha}{2}+n+\frac{1}{2}, m-n-\frac{1}{2} \\ -n+\frac{5}{2}, -n+\frac{1}{2}, 1+m \end{array} \right] \end{aligned}$$

$$I_{T,8} = I_{T_A} S(0,1) \left(\frac{\pi D}{L_0}\right)^{2n+4} \left(\frac{\pi d}{L_0}\right)^{2m-\alpha} \Gamma \left[\begin{array}{c} n+\frac{5}{2}, -m+\frac{\alpha}{2}-2-n, m+2+n \\ 5+n, 3+n, 1+m \end{array} \right].$$

The seventh and eighth two-poles provide series of type C_3 in the same regime, given by

$$C_{3,7} = I_{T_A} \left(\frac{d}{D}\right) \left(\frac{L_0}{\pi d}\right)^{\alpha+1} S(0a) \left(\frac{L_0}{\pi D}\right) \Gamma \left[\begin{array}{c} n+\frac{5}{2}, \frac{\alpha}{2}+n+\frac{1}{2}, -n-\frac{1}{2} \\ -n+\frac{5}{2}, -n+\frac{1}{2}, 1 \end{array} \right], \quad \text{(A.5.5)}$$

and

$$C_{3,8} = I_{T_A} \left(\frac{L_0}{\pi d}\right)^{\alpha} S(0) \left(\frac{\pi D}{L_0}\right)^{2n+4} \Gamma \left[\begin{array}{c} n + \frac{5}{2}, \frac{\alpha}{2} - 2 - n, 2 + n \\ 5 + n, 3 + n, 1 \end{array} \right]. \tag{A.5.6}$$

The steepest-descent contribution for $L_0/\pi d < 1$ is found to be

$$\begin{aligned} I_{T_{SD}}(L_0/\pi d < 1) \approx & \frac{I_{P_A}}{\sqrt{\pi}} \sin\left[2\left(\frac{d}{D}\right)^{\frac{1}{2}}\right] \left(\frac{d}{D}\right)^{\frac{-1}{2}} \left(\frac{L_0}{\pi d}\right)^{\alpha} \\ & \times S(0)\Gamma\left[m + \frac{\alpha}{2}\right] \left(\frac{L_0}{\pi d}\right)^{2m}, \end{aligned} \tag{A.5.7}$$

and the steepest-descent contribution for $L_0/\pi d > 1$ is

$$\begin{aligned} I_{T_{SD}}(L_0/\pi d > 1) \approx & \frac{I_{P_A}}{\sqrt{\pi}} \sin\left[2\left(\frac{d}{D}\right)^{\frac{-1}{2}}\right] \left(\frac{d}{D}\right)^{\frac{1}{4}} \left(\frac{L_0}{\pi d}\right)^{\alpha} \\ & \times S(0)\Gamma\left[m + \frac{\alpha}{2}\right] \left(\frac{L_0}{\pi d}\right)^{2m}. \end{aligned} \tag{A.5.8}$$

The above expressions can be assembled in the same way as in Section A.4 to give the final expression for plane wave tilt phase variance with outer scale as

$$\sigma^2_{\phi,T}(\theta, \alpha) = 4B(\alpha)c_1(\alpha) \int_0^L \mathrm{d}z \frac{\hat{r}_0^{2-\alpha}}{L} \times I_T \tag{A.5.9}$$

where

$$I_T = -\begin{cases} I_{T,1} + I_{T,3} + I_{T_{SD}}\left[L_0/\pi d < 1\right] + C_{3,7} + C_{3,8} & \frac{\pi d}{L_0} > 1 \\ I_{T,4} + I_{T,6} + I_{T,7} + I_{T,8} + I_{T_{SD}}\left[L_0/\pi d > 1\right] & \frac{\pi d}{L_0} < 1, \end{cases} \tag{A.5.10}$$

and the same limitations of Eqs. (A.4.22) apply here as well.

Appendix B

Letters of Permission

B.1 OSA Letter of Permission

The content in Chapters 2 and 3 has been published or is in final preparation for submission in the Journal of the Optical Society of America A (JOSA A). OSA has the following policy regarding republication of this material.

As stated in the OSA Copyright Transfer Agreement, OSA grants to the Author(s) (or their employers, in the case of works made for hire) the following rights:

† The right, after publication by OSA, to use all or part of the Work without revision or modification, including the OSA formatted version, in personal compilations or other publications consisting solely of the Author(s') own works, including the Author(s') personal web home page, and to make copies of all or part of the Work for the Author(s') use for lecture or classroom purposes.

† All proprietary rights other than copyright, such as patent rights.

† If the Work has been prepared by an employee within the scope of his or her employment or as a work made for hire, the right to make copies of the Work for the employer's internal use.

Thus, authors may reproduce figures and text in new publications. The OSA source publication should be referenced.

B.2 SPIE Letter of Permission

The content in Chapter 4 is in final preparation for submission in SPIE Optical Engineering. Optical Engineering has the following policy regarding republication of this material:

As stated in the SPIE Transfer of Copyright agreement, authors, or their employers in the case of works made for hire, retain the following rights: All proprietary rights

other than copyright, including patent rights.

- † The right to make and distribute copies of the Paper for internal purposes.
- † The right to use the material for lecture or classroom purposes.
- † The right to prepare derivative publications based on the Paper, including books or book chapters, journal papers, and magazine articles, provided that publication of a derivative work occurs subsequent to the official date of publication by SPIE.

Thus, authors may reproduce figures and text in new publications. The SPIE source publication should be referenced.